

1 **Impacts of orography and urbanization on extreme**  
2 **precipitation event in Beijing during 2023**

3

4 Haobo Cui<sup>1</sup>, Hongyong Yu<sup>1</sup>, Xingshuo Zuo<sup>1</sup> and Guocan Wu<sup>1\*</sup>

5

6 <sup>1</sup>State Key Laboratory of Earth Surface Processes and Disaster Risk Reduction,  
7 Faculty of Geographical Science, Beijing Normal University, Beijing, 100875 China

8

---

*\*Corresponding author: Guocan Wu*

*E-mail address: gcwu@bnu.edu.cn*

9 **Abstract**

10 The effects of urbanization and orographic uplift play significant roles in extreme  
11 precipitation events, and therefore in water management. In this study, the main  
12 impact factors in an extreme precipitation event that occurred during July 2023 in  
13 Beijing were analyzed, using the Weather Research and Forecasting (WRF) model.  
14 The results showed that the main cause of this precipitation event was the residual  
15 forces of Typhoon Doksuri combined with water vapor transported from the  
16 subtropical high. The orographic effect altered the spatial pattern of accumulated  
17 precipitation throughout the simulation period by changing the local circulation, as the  
18 accumulated precipitation in the southwestern mountainous regions increased by  
19 229.4 mm (41.34%), and the precipitation in the plain areas decreased by 83.6 mm  
20 (43.50%). The impact of the underlying urban surface led to accumulated  
21 precipitation in the southwestern mountainous regions of Beijing decreasing by 88.1  
22 mm (15.87%). Further analysis showed that orographic features caused the uplift of  
23 air masses in the mountainous regions and prevented the low-pressure system from  
24 propagating, leading to significant enhancement of the convective intensity over  
25 Beijing and precipitation for a prolonged duration. The presence of urban surfaces  
26 contributed to reductions in the latent heat flux and wind speed, resulting in decreased  
27 energy transfer to the southwestern mountainous regions via easterly winds. This  
28 reduction in energy suppressed convective activity and subsequently led to a decrease  
29 in precipitation in these regions. As extreme precipitation events become more  
30 frequent, the comprehensive research into such events may help with prevention and  
31 the response to similar events in the future.

32 **Keywords:** WRF model; Precipitation simulation; orographic impacts; Urbanization;  
33 Beijing area

34

## 35 **1. Introduction**

36 In the precipitation process, water vapor in the atmosphere condenses and falls to  
37 the Earth's surface in the form of liquid or solid as a crucial component of the global  
38 water cycle (Gimeno et al. 2010; Trenberth et al. 2003). Unlike other climatic  
39 variables, precipitation is typically discontinuous in a given location and its temporal  
40 distribution is uneven (Pendergrass and Knutti 2018; Wu et al. 2021). Extreme  
41 precipitation events, characterized by high precipitation rates over short durations or  
42 prolonged accumulated precipitation, often result in natural disasters such as floods  
43 and landslides. These events can disrupt ecosystems, agricultural production, and  
44 cause significant economic damage and loss of life (Ayat et al. 2022; Mahoney 2016;  
45 Yu et al. 2024). Therefore, extreme precipitation has become a major focus of  
46 research in weather and climate research (Dai et al. 2024; Li et al. 2024a; Sun et al.  
47 2021; Zhang et al. 2022).

48 **Orography** is one of the most critical factors in land-air interaction, due to its  
49 capacity to alter precipitation patterns through a variety of complex processes (Smith  
50 2006). **Mountains** can modify the spatial distribution of precipitation by blocking and  
51 uplifting air masses to alter the atmospheric properties at different elevations on both  
52 the windward and leeward sides (Cornejo et al. 2024; Davolio et al. 2009; Lin et al.  
53 2001; Wei et al. 2023). **Meanwhile**, orographic forcing can also influence the  
54 temperature and humidity of the lower atmosphere, which alters the distribution of  
55 convection by controlling the buoyancy of air masses to increase the moisture content  
56 over the foothills, thereby promoting precipitation in these regions (Du et al. 2020;  
57 Gao et al. 2021; Nicolas and Boos 2024; Xia and Zhang 2019; Yin et al. 2020). In  
58 addition, the thermodynamic differences between mountainous areas and plains give  
59 rise to local thermal circulations, which are among the physical processes that  
60 influence the spatial distribution and diurnal variation of precipitation (Chen et al.  
61 2014; He and Zhang 2010). **The altitude used** in the numeric model can affect the  
62 regional water vapor flux, especially the channel of moisture in the lower and middle  
63 troposphere (Saurral et al. 2015). Therefore, the influence of **orography** is particularly

64 significant for determining precipitation patterns in mountainous regions and  
65 surrounding plains.

66 Due to human activities, altered land use patterns caused by urbanization are  
67 **another** key factor that **needs** to be considered in precipitation events (Dou et al. 2015;  
68 Huang et al. 2019; Niyogi et al. 2011). The emergence of urban areas has led to the  
69 development of unique urban canopies and urban boundary layers, giving rise to the  
70 urban heat island (UHI) effect, thereby causing convergence and upward lifting in the  
71 lower atmosphere (Bornstein and Lin 2000; Hjelmfelt 1982). The UHI effect can  
72 enhance boundary layer turbulence mixing by increasing the surface heat flux to  
73 strengthen boundary layer instability and lead to precipitation (Holst et al. 2016; Nie  
74 et al. 2017). This effect is especially significant for mesoscale and small-scale  
75 circulations and convection (Dixon and Mote 2003; Oke 1982; Yin et al. 2020; Zhang  
76 et al. 2017), which induces convective activity in urban and surrounding areas, and  
77 changes in precipitation patterns (Fu et al. 2024; Li et al. 2011; Yang et al. 2017).  
78 **However**, precipitation **respond** to urbanization varies under different degree of land  
79 use change climatic backgrounds (Wang et al. 2015). The “urban rain island” effect  
80 may be observed in some coastal cities with abundant moisture transport (Jauregui  
81 and Romales 1996; Wang et al. 2018), whereas the depletion of moisture in the lower  
82 atmosphere caused by urban activities may lead to the “urban dry island” effect in  
83 relatively arid cities (Freitag et al. 2018; Wang and Gong 2010). Therefore, the  
84 mechanisms that urbanization influences extreme precipitation events are complex,  
85 necessitating further research to clarify the roles of cities in these events.

86 Beijing is located in the northwest of the North China Plain, **where is the**  
87 **transitional zone between the Taihang Mountains, Yanshan Mountains, and North**  
88 **China Plain.** It is an international metropolis with a population of over 10 million and  
89 its surrounding areas have experienced rapid urbanization since the 1980s. In recent  
90 years, Beijing and neighboring areas of Hebei and Tianjin have frequently  
91 experienced high-intensity extreme precipitation events during the summer months  
92 (Tewari et al. 2022; Yu et al. 2017; Zhang et al. 2013b; Zhong et al. 2015). Some

93 previous studies have provided evidence of increases in the frequency of extreme  
94 precipitation events in large cities (Liang and Ding 2017), and Beijing is a  
95 representative region for studying these events.

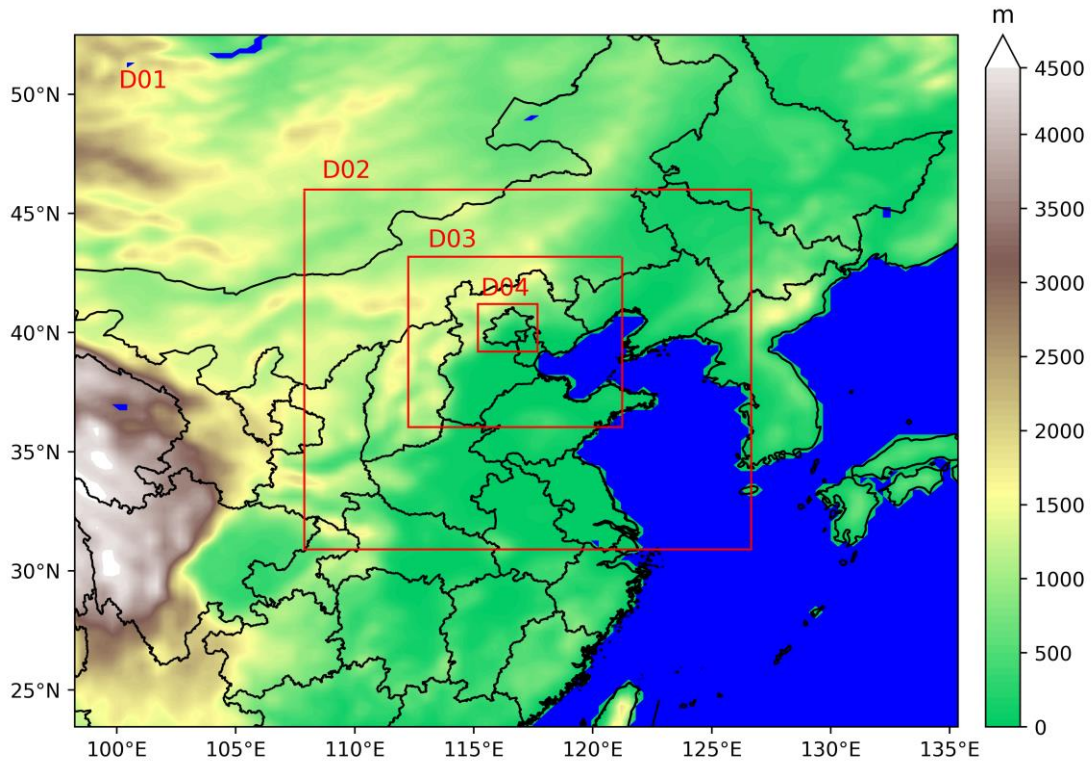
96 In this study, an extreme precipitation event that occurred in Beijing from July 29  
97 to August 2, 2023 was analyzed, using the Weather Research and Forecasting model  
98 (WRF). The accumulated precipitation distribution had a clear pattern, with higher  
99 amounts in the southwestern mountainous areas and lower amounts in the  
100 northeastern regions. Therefore, both the orographic effect and urban land use could  
101 have potentially influences to the precipitation spatial pattern, which were assessed by  
102 the comparisons of several experiment schemes. The causes of the event and the  
103 related mechanisms were examined, by quantifying the effects of orography, land use,  
104 and other factors on the precipitation event.

105

## 106 **2. Data and Methodology**

### 107 2.1. Study Area and Precipitation Event

108 The present study focused on the “23·7” precipitation event that occurred in  
109 Beijing area (shown in region D04 in Figure 1) during July 2023. From July 29 to  
110 August 2, 2023, a severe and prolonged heavy rainfall event affected Beijing and  
111 neighboring areas of Tianjin and Hebei. This event was driven by the residual forces  
112 of Typhoon Doksuri moving northward and the influence of Typhoon Khanun. The  
113 average precipitation in the Beijing region exceeded 300 mm, where the most affected  
114 areas, including Fangshan and Mentougou districts, recorded average accumulated  
115 rainfall amounts greater than 500 mm (Li et al. 2024c). The rainstorm also triggered  
116 severe flooding and urban waterlogging, resulting in significant damage to  
117 infrastructure and property across the entire region.



118

119 **Figure 1:** Study area and domains of the numerical model. The coordinates of the different  
 120 domains are as follows: D01: 98.23 E to 135.35 E, 23.45 N to 52.49 N; D02: 107.88 E to  
 121 126.65 E, 30.91 N to 46.00 N; D03: 112.25 E to 121.23 E, 36.04 N to 43.19 N; D04: 115.17 E  
 122 to 117.68 E, 39.21 N to 41.20 N. The grid spacing for each domain is 27 km, 9 km, 3 km, and 1  
 123 km, respectively.

124

## 125 2.2. Data Descriptions

126 In the experiment, ERA5 global reanalysis data were used to provide initial and  
 127 boundary conditions for the WRF model (Hersbach et al. 2020b). The data selected  
 128 for this study has a temporal resolution of 1 hour and a spatial resolution of  $0.25^\circ \times$   
 129  $0.25^\circ$ . To investigate the impact of land use in the simulation, updated land use data  
 130 were used to replace the default one within the WRF model. The data used in this  
 131 study were acquired from the Moderate-resolution Imaging Spectroradiometer  
 132 (MODIS) MCD12Q1 V6 product for the year of 2020, with a spatial resolution of 500  
 133 m (Friedl 2019).

134 The gauge observations used to verify the model simulation on single points  
 135 were from the China Meteorological Administration (version 2.0;  
 136 <http://data.cma.cn/en>). There are totally 37 stations in the D04 area, shown in Figure

137 2(a). Due to the scarcity of meteorological stations, the observations were compared  
138 with the model outputs on the grid that the meteorological stations located in. In order  
139 to evaluate the quality of simulated precipitation depending on terrain, the stations  
140 with altitude greater or smaller than 100 m are divided into mountainous stations and  
141 plain stations, which have 10 and 27 stations respectively.

142 The analysis involves the movement and spatial variability of extreme  
143 precipitation systems, which cannot be adequately captured by meteorological  
144 observation stations. Alternatively, satellite-derived precipitation products are  
145 commonly used and have reliabilities in estimating spatial precipitation distribution  
146 (Bhattarai and Talchabhadel 2024). Among them, the Climate Prediction Center  
147 Morphing technique (CMORPH) product can offer high temporal and spatial  
148 resolution and has demonstrated advantages in capturing extreme precipitation  
149 patterns (Liu et al. 2022), which has been validated over China in previous studies  
150 (Ebert et al. 2007; Jiang et al. 2016; Sun et al. 2016). CMORPH data based on a  
151 combination of microwave and infrared precipitation data provide high temporal and  
152 spatial resolution global precipitation data (Joyce et al. 2004), and is highly  
153 reasonable to be used to validate the simulation results. In this study, CMORPH data  
154 with a temporal resolution of 30 min and spatial resolution of 8 km  $\times$  8 km were used  
155 for precipitation validation.

156

### 157 2.3. Model Description and Experimental Design

158 WRF model version 4.5.1 was selected as the numerical simulation tool for this  
159 study (Skamarock 2019). The simulation period covered from 00:00 UTC July 28<sup>th</sup>,  
160 2023 to 00:00 UTC August 2<sup>nd</sup>, 2023, while the first 24 hours were used for model  
161 spin-up. A four-level nested domain was utilized with grid spacing (grid number) of  
162 27 km (120  $\times$  122), 9 km (181  $\times$  187), 3 km (259  $\times$  268), and 1 km (217  $\times$  226).  
163 Domain D01 covered most of central and eastern China, and domain D04 was focused  
164 on the Beijing region (Figure 1). In addition, 49 vertical layers were employed in the  
165 simulation and the upper boundary was set at 50 hPa to resolve the vertical structure

166 of the subtropical high and upper-level jet streams while minimizing spurious wave  
 167 reflection near the upper boundary (Wang et al. 2018, Yu et al. 2024, Pei et al. 2025).  
 168 The physical packages used are summarized in Table 1. To ensure that the large-scale  
 169 circulation in the experiment closely matched the ERA5 input data for accurate results,  
 170 spectral nudging was applied to the D01 domain in terms of the zonal and meridional  
 171 wind, temperature, and specific humidity (Miguez-Macho et al. 2004; Spero et al.  
 172 2014). The assimilation coefficient was set to  $3 \times 10^{-4} \text{ s}^{-1}$  suggested in other previous  
 173 researches (Holst et al. 2016; Liu et al. 2012; Ma et al. 2016; Pei et al. 2025), and the  
 174 cut-off wave number was set to 3 in both the zonal and meridional directions as the  
 175 length-scale is more accurate at 1000 km (Gómez and Miguez-Macho 2017; Kukulies  
 176 et al. 2023). The hourly output for region D04 was used in the following analysis.

177

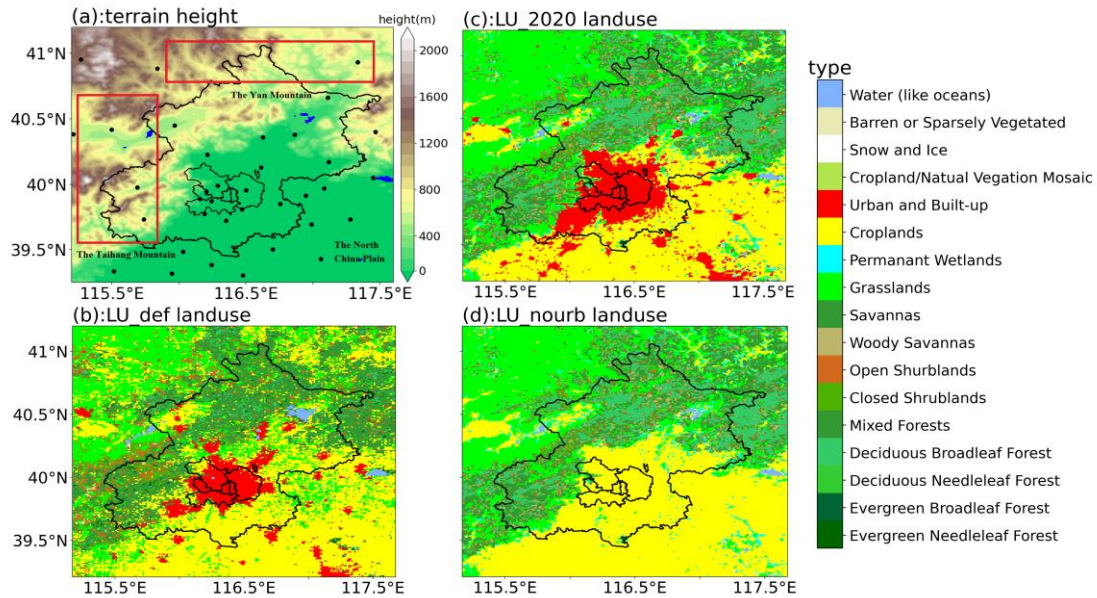
178

179

**Table 1:** Model configurations selected for WRF in this study

Options	Settings
Surface layer scheme	Mellor-Yamada-Janjic scheme (Janjić 1994)
PBL scheme	Yonsei University scheme (Hong et al. 2006)
Land Surface scheme	unified Noah land-surface model (Chen and Dudhia 2001)
Shortwave radiation	Dudhia scheme (Dudhia 1989)
Longwave radiation	RRTM scheme (Mlawer et al. 1997)
Microphysics scheme	WSM6 (Hong 2006)
Cumulus scheme	Kain-Fritsch scheme for D01 & D02 (Kain 2004)

180



181  
 182 **Figure 2:** Terrain elevation and land use types in domain D04 in the experiment. (a) Terrain  
 183 elevation in region D04. The dots represent the locations of meteorological stations used in this  
 184 study. (b) Default land use types in region D04. (c) Land use types in region D04 after  
 185 replacement. (d) Land use types in region D04 with urban areas replaced by cropland.

186

187 To improve the accuracy when simulating the impacts of urban areas on the  
 188 precipitation event, the single-layer urban canopy model (Chen et al. 2011) was used  
 189 to enhance the accurate simulation of the evolution of dynamic and thermodynamic  
 190 processes in urban environments (He et al. 2023; Yu and Liu 2015). Different  
 191 sensitivity test groups were set-up to explore the effects of land use and orography on  
 192 the precipitation event, and the differences between these test groups were analyzed.  
 193 The default land use types in WRF (represented as LU\_def in Figure 2(b)) were  
 194 replaced with land use data from the MODIS MCD12Q1 V6 product for the year  
 195 2020 (represented as LU\_2020 in Figure 2(c)).

196 To explore the impact of orography, based on the LU\_2020 scheme, areas in  
 197 domain D03 and D04 with elevations greater than 100 m were set to 100 m  
 198 (represented as LU\_nohgt) in order to explore the impacts of the Taihang and Yan  
 199 Mountains on precipitation. In addition, urban areas in the land use data were replaced  
 200 with cropland (represented as LU\_nourb in Figure 2(d)) to examine the results in the  
 201 absence of urban surface effects.

202

## 203 2.4. Verification Statistics

204 To investigate the impacts of land use changes on the simulation results, the  
205 accumulated precipitation, precipitation intensity from LU\_2020 simulations with  
206 [validated](#) data were analyzed. The following evaluation metrics were used for  
207 validation: mean absolute error (MAE), root mean square error (RMSE), and  
208 correlation coefficient (R). The specific formulas for these metrics are as follows:

$$209 \quad MAE = \frac{1}{n} \sum_{i=1}^n |S_i - O_i| \quad (1)$$

$$210 \quad RMSE = \sqrt{\frac{\sum_{i=1}^n (S_i - O_i)^2}{n}} \quad (2)$$

$$211 \quad R = \frac{\sum_{i=1}^n (S_i - \bar{S})(O_i - \bar{O})}{\sqrt{\sum_{i=1}^n (S_i - \bar{S})^2 \sum_{i=1}^n (O_i - \bar{O})^2}} \quad (3)$$

212 where  $S_i$  and  $O_i$  are the simulated and observed values, respectively;  $\bar{S}$  and  $\bar{O}$  are the  
213 average values of the simulated and validated data, respectively; and  $n$  is the number  
214 of grid points.

215

## 216 3. Results

### 217 3.1. Evolution of the Precipitation Event

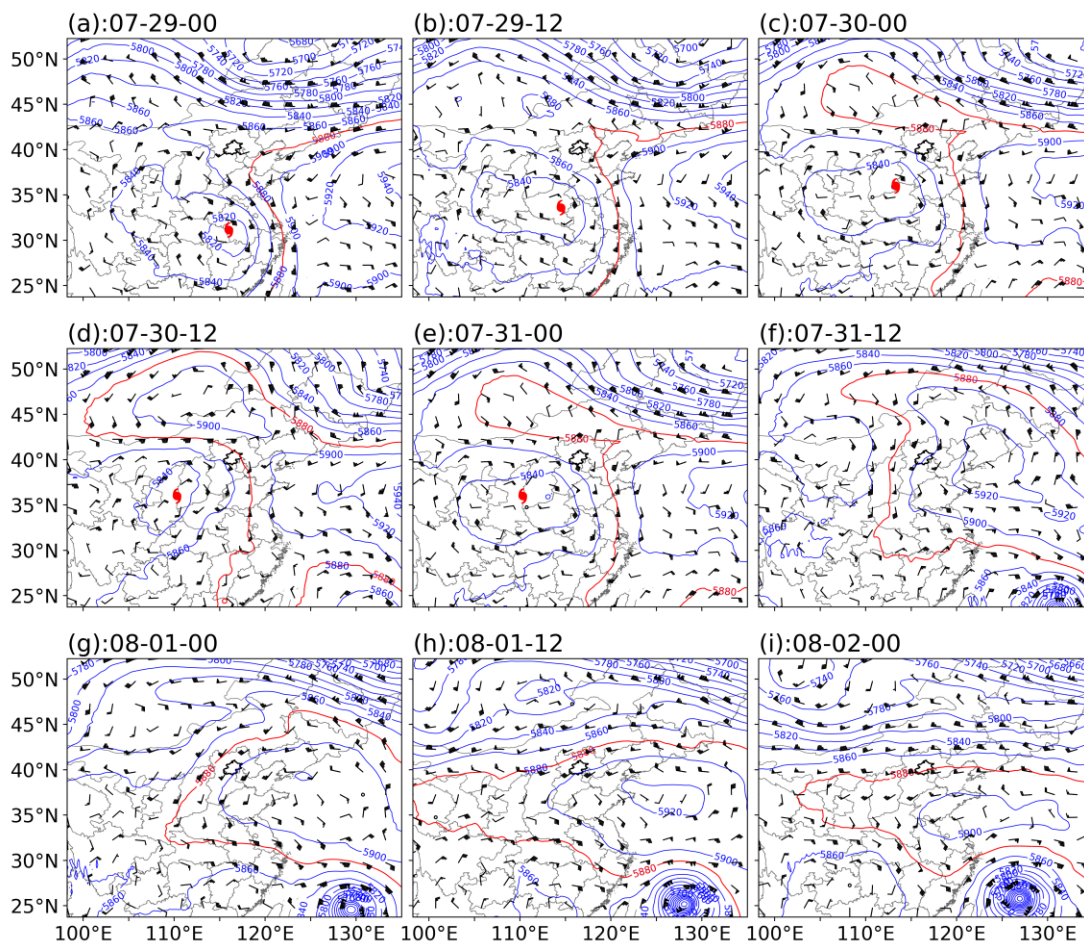
218 As shown in Figure 3, the remnant low of Typhoon Doksuri maintained  
219 considerable intensity at the 500-hPa level on July 29, with its center located near  
220 112 °–114 °E, 32 °–34 °N. At this time, the main body of the Western Pacific  
221 Subtropical High (WPSH) was situated along the eastern coastal region of China and  
222 the adjacent seas, with the westernmost position of the 5880-gpm geopotential height  
223 contour around 118 °E, indicating its limited westward extension. The Beijing area  
224 was primarily located within the weakly influenced northwestern periphery of the  
225 WPSH, where low-level moisture transport was relatively weak and heavy  
226 precipitation had not developed.

227 By July 30, the WPSH had extended westward, with the 5880-gpm contour  
228 reaching approximately 105 °–110 °E and stretching northward to Mongolia. It thereby  
229 established a relatively stable high-pressure ridge to the north of the Doksuri remnant  
230 low and formed a typical blocking circulation pattern. Consequently, the center of the  
231 remnant low oscillated slightly within 112 °–115 °E and 33 °–35 °N, illustrating a  
232 pronounced quasi-stationary state that persisted until around 12:00 UTC July 31.  
233 During this period, Beijing was located between the southern of the blocking high and  
234 the northern of the remnant low. This configuration was favorable for sustained  
235 southeast flow and continuous moisture toward Beijing area.

236 After 12:00 UTC July 31, the remnant low of Doksuri gradually weakened and  
237 shifted slightly westward, while the blocking high also began to decay. Meanwhile,  
238 Typhoon Khanun over the offshore waters of China (Figures 3(f)–(i)) established a  
239 strong cyclonic circulation on its northwestern side, further enhancing moisture  
240 transport into North China. It greatly increased precipitable water, thereby triggered  
241 the heavy precipitation event between 12:00 UTC July 31 and 00:00 UTC August 1.  
242 Then, the WPSH further intensified and continued to westward extension, with the  
243 5880-gpm contour maintained at the west of 108 °E. The western ridge of the  
244 strengthened WPSH subsequently blocked the moisture transport pathway from  
245 Typhoon Khanun toward North China, leading to a pronounced reduction in the  
246 moisture transportation. The precipitation process then gradually weakened and  
247 terminated.

248 The differences among the experimental groups are mainly reflected in the local  
249 circulation. A comparison of Figures S1 and S2 shows that the removal of terrain  
250 elevation exerts a noticeable influence on the circulation associated with the remnant  
251 low-pressure system. In the absence of the orographic blocking effect of the Taihang  
252 Mountains, the remnant low of Typhoon Doksuri continued to move northward and  
253 prolonged the duration of the low-pressure circulation. Consequently, the changed  
254 dynamical and thermal conditions over the Beijing region were prone to alter the  
255 spatiotemporal distribution of precipitation. In comparison, the differences between

256 Figures S1 and S3 indicate that urban underlying surface has a relatively weak effect  
 257 on the large-scale circulation. It resulted in the reduction of the regional surface  
 258 roughness and an increase in wind speed over Beijing area. In addition, the dissipation  
 259 time of the remnant low circulation in the LU\_nourb scheme is slightly prolonged due  
 260 to the reduction of anthropogenic heat. Therefore, the large-scale circulation pattern in  
 261 the LU\_nohgt and LU\_nourb schemes are generally similar to LU\_2020. This  
 262 suggests that the differences in simulated precipitation are primarily induced by the  
 263 changes in local circulation.



264  
 265 **Figure 3:** 500hpa circulation pattern for the precipitation event (source: ERA5). The blue solid  
 266 lines represent geopotential height contours; the red solid contours represent position of  
 267 subtropical high; the typhoon symbols in (a) - (e) represent residual circulation center of typhoon  
 268 Doksuri.

## 270 3.2. Analysis of Variations in Precipitation

### 271 3.2.1. Impacts of Updated Land Use Data

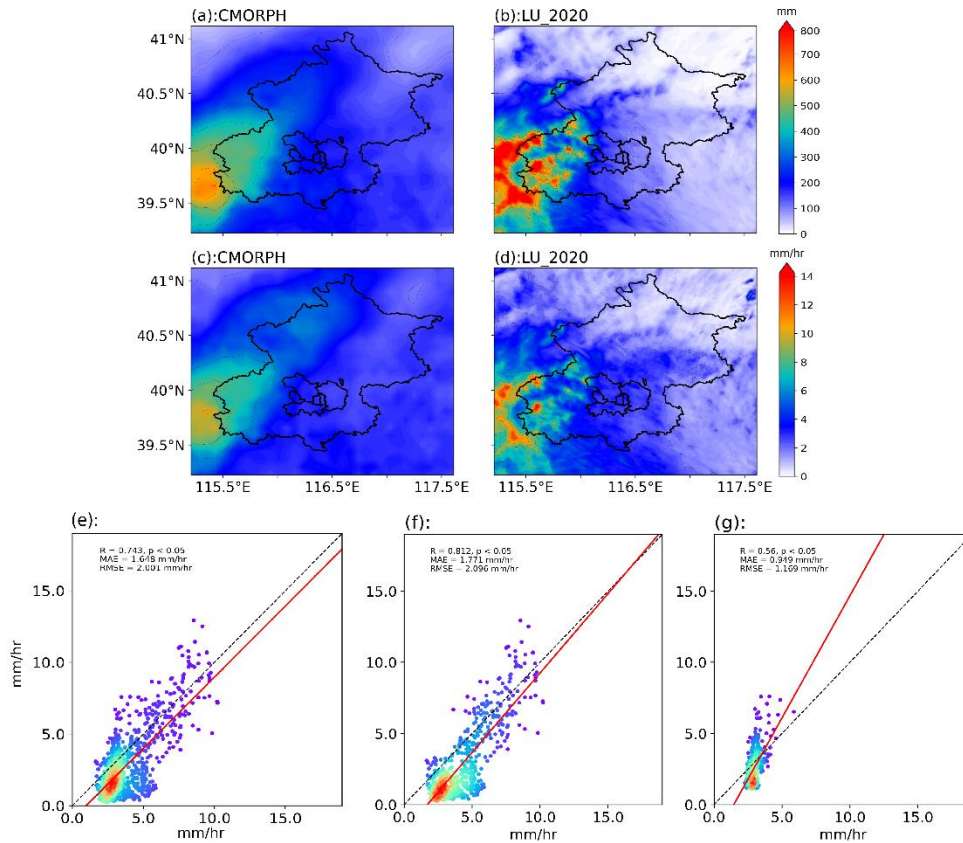
272 The simulated precipitation was compared with meteorological station

273 observations and satellite products to evaluate the accuracy of the model outputs. It  
274 was found that, the maximum observed precipitation is 772.2 mm, which was  
275 comparable with the simulation result of approximate 800.0 mm. The average  
276 precipitation amount was 237.0 mm for all the station observations during this  
277 precipitation event, and the average simulated value on the grid where the station  
278 located in is 228.4 mm. Therefore, the magnitudes were comparable between model  
279 simulation and observation on the stations.

280 The CMORPH data were used to further verify the spatial distribution of  
281 precipitation on D04 region. As shown in Figure 4(a–b), the spatial distributions of  
282 accumulated precipitation were similar, with higher precipitation in the southwestern  
283 mountainous areas and lower precipitation in the northeastern region. This illustrated  
284 that the pattern of LU\_2020 scheme closely matched the accumulated precipitation  
285 distribution obtained by CMORPH, which was slightly higher than 700 mm. The  
286 simulated average precipitation intensity results also matched closely with the spatial  
287 distribution of CMORPH (Figure 4(c-d)) although LU\_2020 slightly underestimated  
288 the precipitation intensity (Figure 4(e)). Thus, the WRF simulation results provided a  
289 reasonable representation of the overall precipitation event, and the LU\_2020  
290 simulation results were used to analyze the differences due to orography and land use.  
291 The correlation coefficient of the plain areas shows a smaller value ( $R=0.56$ )  
292 compared with mountain areas ( $R=0.81$ ). For the result of MAE and RMSE, the  
293 statistics in the plain areas are smaller than those in the mountainous areas and the  
294 entire study region (Table 2). This may be due to that there are more stations in the  
295 plain areas, and the precipitation is smaller than mountain areas.

296 In addition, the model uncertainty was further accessed using an ensemble  
297 simulation of LU\_2020 scheme, where are originated from 10 ensemble members of  
298 ERA5. They provide estimates of the short-range forecast uncertainty, and can be  
299 considered to represent the evolution of the errors in the high-resolution component of  
300 ERA5 (Hersbach et al. 2020a). The results show that there is slightly difference  
301 between the ensemble mean simulation and our experimental results (Figure S4).

302 Statistically, the average precipitation intensity is 3.6 mm/hr for LU\_2020 scheme and  
 303 4.1 mm/hr for the ensemble mean. The RMSE and MAE of precipitation intensity is  
 304 1.17 mm/hr and 0.86 mm/hr for the two simulation results and the correlation  
 305 coefficient is 0.90. Therefore, the experimental scheme and simulation results in this  
 306 study are convincing.



307  
 308 **Figure 4:** Comparison of simulated and validated precipitation: (a)–(b) accumulated precipitation  
 309 for CMORPH and LU\_2020, respectively; (c)–(d) average precipitation intensity for CMORPH  
 310 and LU\_2020; and (e) scatter plots for the precipitation intensity for CMORPH in *x* axis and  
 311 LU\_2020 in *y* axis, while the red line represents the linear regression; (f) and (g) representing area  
 312 where terrain height greater and smaller than 100 m.

313  
 314

Table 2: Statistics of the precipitation intensity between simulation and CMORPH data.

	R	RMSE (mm/hr)	MAE (mm/hr)
All	0.74	2.00	1.65
Mountain	0.81	2.10	1.77
Plain	0.56	1.17	0.95

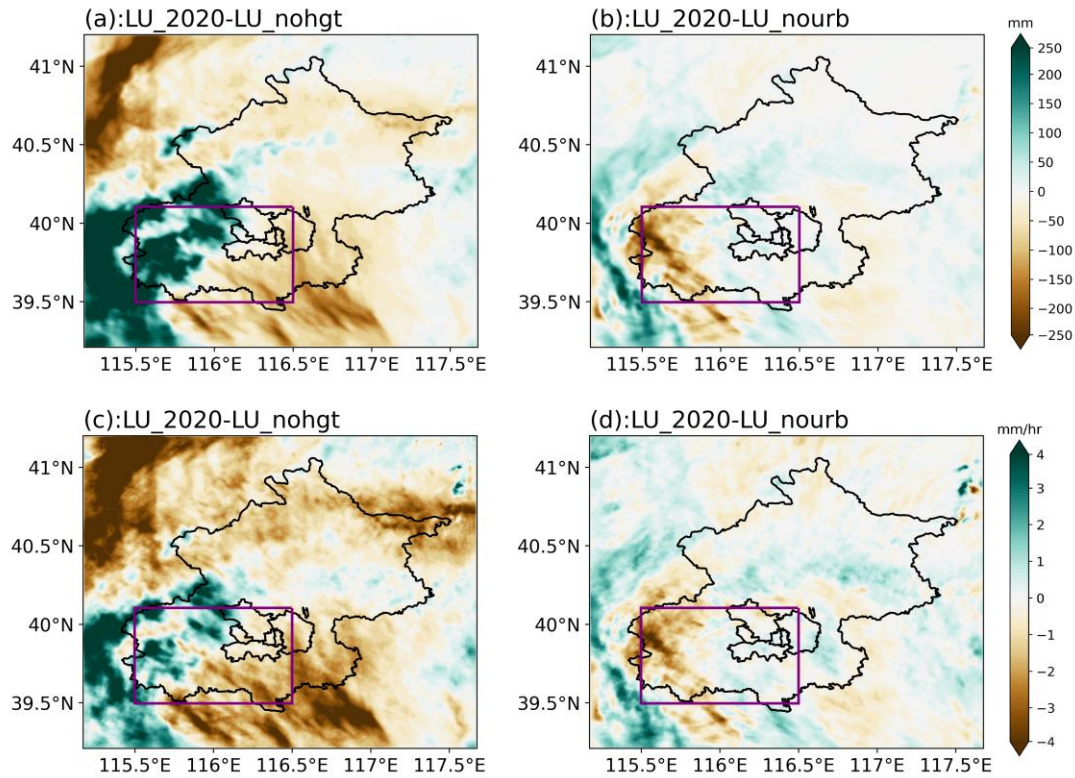
315  
 316

### 317 3.2.2. Impacts of Orography

318 Figure 5 (a) and 5(c) show the spatial distributions of the average precipitation

319 intensity and accumulated precipitation before and after removing the orography. It  
320 illustrated that the removal of terrain elevation indeed significantly altered the spatial  
321 pattern of accumulated precipitation throughout the simulation period. Compared to  
322 the LU\_2020 scheme, the LU\_nohgt exhibited a marked decrease in cumulative  
323 precipitation over the southwestern portion of D04 area. The accumulated  
324 precipitation was 229.4 mm higher in LU\_nohgt, accounting for over 41.34% of the  
325 total precipitation. In contrast, in the central urban and northern regions of Beijing, the  
326 total precipitation was 83.6 mm lower, representing 43.50% of the total precipitation.  
327 This is primarily attributed to the removal of the Taihang mountainous region. As the  
328 blocking effect caused by mountain on the remnant circulation was greatly diminished.  
329 This allowed low-pressure system persist a long period within Beijing region and  
330 facilitated its northward progression. The lack of orographic lifting ultimately leads to  
331 different precipitation distributions over the Beijing region.

332 Figure 6(a) and 6(b) show the changes in precipitation for each time period at the  
333 central latitudes between 39.5°N and 40.1°N. From 00:00 to 10:00 on July 30,  
334 precipitation primarily occurred in the transition zone between the city and mountains,  
335 where the terrain features caused heavy precipitation in the mountainous areas in the  
336 morning during this period. From July 31 to 12:00 on August 1, precipitation mainly  
337 occurred in the mountainous areas, and the impact of orography became more  
338 significant. In the LU\_nohgt scheme, precipitation in the mountainous areas stopped  
339 around 12:00 on July 31, whereas in the LU\_2020 scheme, precipitation continued  
340 until around 00:00 on August 1, i.e., 12 hours longer. Thus, the topography had a  
341 significant impact on the second phase of precipitation. In terms of the precipitation  
342 intensity and distribution, the presence of the orography altered the timing of heavy  
343 precipitation in the mountainous areas and intensified the precipitation in the central  
344 urban area around 12:00 on July 31.



345  
 346 **Figure 5:** Effects of terrain and urban underlying surface changes on accumulated precipitation  
 347 and average precipitation intensity from 00:00 July 29<sup>th</sup> to 00:00 UTC August 2<sup>nd</sup>: (a) and (c)  
 348 differences in accumulated precipitation and average precipitation intensity between the  
 349 simulation using 2020 land use data and the scheme where terrain higher than 100 m was removed;  
 350 and (b) and (d) differences in accumulated precipitation and average precipitation intensity  
 351 between the simulation using 2020 land use data and the scheme where urban land use was  
 352 removed. The purple area (RegP) indicates the region in Beijing where the difference in  
 353 precipitation was significant.

354

### 355 3.2.3. Impacts of Land Use

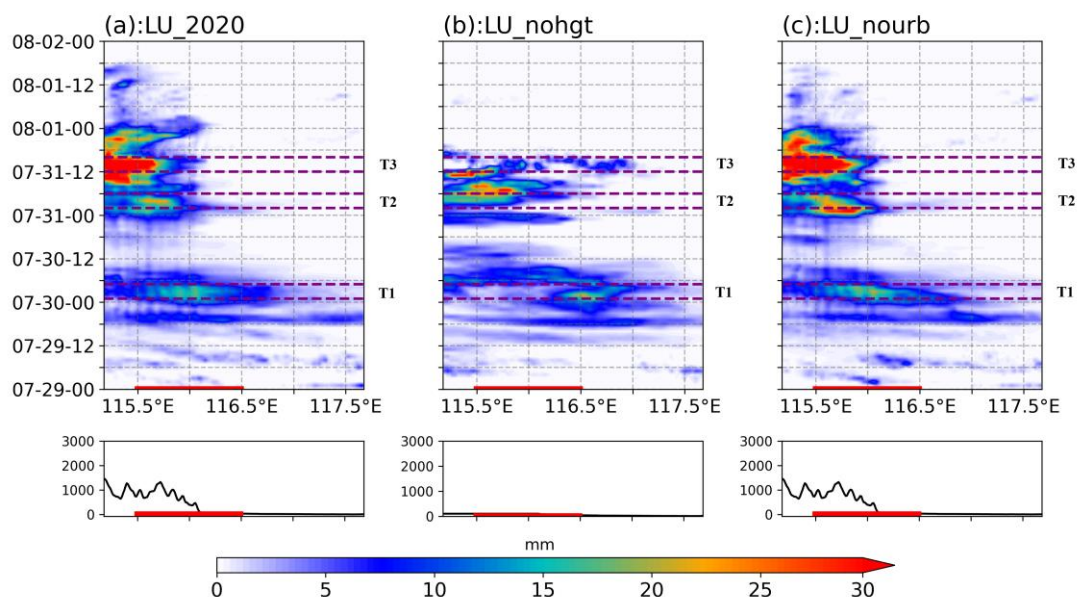
356 Figure 5(b) and 5(d) show the impact of the urban land surface compared with  
 357 removal of the urban land surface. The spatial distributions of the average  
 358 precipitation intensity and accumulated precipitation were quite similar **between**  
 359 LU\_2020 and LU\_nourb, with no significant difference in the overall precipitation  
 360 pattern. The presence of urban areas did not significantly affect the central urban  
 361 region of Beijing. However, in the southwestern mountainous region of Beijing, the  
 362 average accumulated precipitation was 88.1 mm lower (the total precipitation was  
 363 15.87% lower).

364 Figure 6(a) and 6(c) show the variations in precipitation with longitude and time

365 for the central urban region corresponding to the central latitude. From 00:00 to 10:00  
 366 on July 30, the range and intensity of precipitation differed little between the city and  
 367 the **mountain** transition zone, indicating that changes in land use had minor effects  
 368 during this period. From July 31 to 12:00 on August 1, the overall total precipitation  
 369 was lower in the LU\_2020 scheme, although more precipitation occasionally occurred  
 370 in the western part of the city in the LU\_2020 scheme compared with the LU\_nourb  
 371 scheme. There was no significant difference in the duration of precipitation between  
 372 the two experimental groups.

373 Therefore, during the precipitation event, both **orography** and land use altered the  
 374 precipitation pattern, where the most significant changes in precipitation occurred in  
 375 the southwestern part of Beijing. To understand the main causes of the differences in  
 376 precipitation, the region denoted by the purple box in Figure 5 **was selected** for more  
 377 detailed analysis of the **underlying** mechanism as it was affected most by the land  
 378 surface (referred to as RegP **hereinafter**). In addition, due to the prolonged nature of  
 379 the event, three time periods with notable differences in the precipitation distribution  
 380 according to Figure 5 were selected for further mechanistic analysis to explore the  
 381 effects of **orography** and land use on the event. The three periods of interest were:  
 382 01:00–04:00 UTC on July 30<sup>th</sup> (referred to as T1), 03:00–06:00 UTC on July 31<sup>st</sup>  
 383 (referred to as T2), and 12:00–15:00 UTC on July 31<sup>st</sup> (referred to as T3).

384



385

386 **Figure 6:** Hovmöller diagrams from 00:00 July 29<sup>th</sup> to 00:00 UTC August 2<sup>nd</sup> for the three  
387 experimental groups: (a) LU\_2020 scheme, (b) LU\_nohgt scheme, and (c) LU\_nourb scheme,  
388 within the range of 39.8 N–40.1 N. Terrain heights at corresponding latitudes are shown.

389

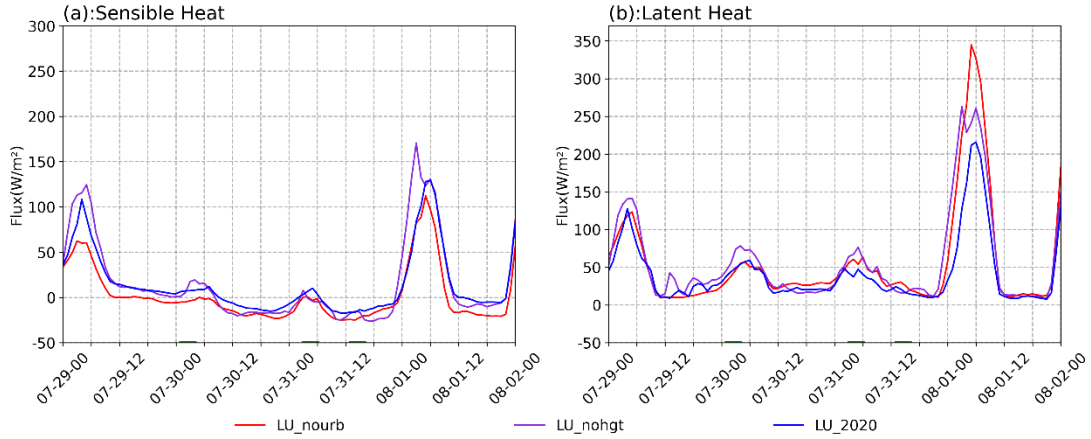
### 390 3.3. Physical Mechanism

#### 391 3.3.1. Energy and Water Vapor Budget Comparison

392 **The** energy and water vapor fluxes were compared among different experimental  
393 groups. As shown in Figure 7, all experimental groups exhibited distinct diurnal  
394 variations, with significant increases in both the sensible heat flux and latent heat flux  
395 after 00:00 UTC August 1<sup>st</sup>. This phenomenon was mainly due to the end of the  
396 extreme precipitation event, where the increased surface energy input strengthened  
397 both the sensible and latent heat fluxes. In RegP, both the sensible and latent heat  
398 fluxes were slightly higher than the regional averages. The **orographic** effects on the  
399 latent heat flux were more pronounced, especially during periods T1 and T2 (Table 3),  
400 as the removal of **orographic** features **lead** to an increase in both surface pressure and  
401 temperature for the high elevated regions. It enhances near-surface humidity and  
402 alters the latent heat flux across the region. The relatively lower latent heat flux  
403 observed in LU\_nohgt during period T3 could be attributed to the extended duration  
404 of the precipitation event, **which was** caused by the removal of **orography**.

405 Compared with period T1, **urbanization reduced latent heat flux by an average** of  
406 16.70 W/m<sup>2</sup> and 7.06 W/m<sup>2</sup> in RegP during periods T2 and T3, respectively. **This was**  
407 mainly **because** the lower permeability of urban surfaces compared with croplands  
408 reducing the regional humidity, and thus decreasing the latent heat flux across the area.  
409 **The** impact of urbanization on the moisture content in RegP was less pronounced  
410 **during** period T1, suggesting that removing urban areas had minimal effect on the  
411 water vapor content. Changes in the sensible heat flux (Figure 7(a)) due to  
412 urbanization were also concentrated in RegP, **since the orography** in the urban area  
413 varied little **among** the three experimental groups. When the land use shifted from  
414 urban surfaces to croplands, the reduced urban heat emissions significantly decreased  
415 the sensible heat flux in the central urban area, so it was lower than **that** in the other

416 groups. It was notable that changes in the latent heat flux (Figure 7(b)) in RegP were  
 417 more complex than those in the sensible heat flux, which could be attributed to  
 418 different changes in the water vapor content.



419  
 420 **Figure 7:** Temporal variations in energy balance during the event for the LU\_2020, LU\_nohgt,  
 421 and LU\_nourb schemes. In (a) and (b), solid lines represent the sensible and latent heat fluxes  
 422 within the precipitation anomaly area RegP for each scheme.

423  
 424  
 425

**Table 3:** Average flux values in RegP region during precipitation process (unit:  $W/m^2$ )

flux	Scheme	T1	T2	T3	All-time
Sensible Heat	LU_2020	7.28	5.98	-15.36	14.04
	LU_nohgt	10.85	-0.62	-18.47	16.25
	LU_nourb	-4.19	-0.92	-22.91	1.83
Latent Heat	LU_2020	46.38	41.82	19.04	41.85
	LU_nohgt	63.38	67.18	17.68	58.00
	LU_nourb	42.74	58.52	26.10	56.29

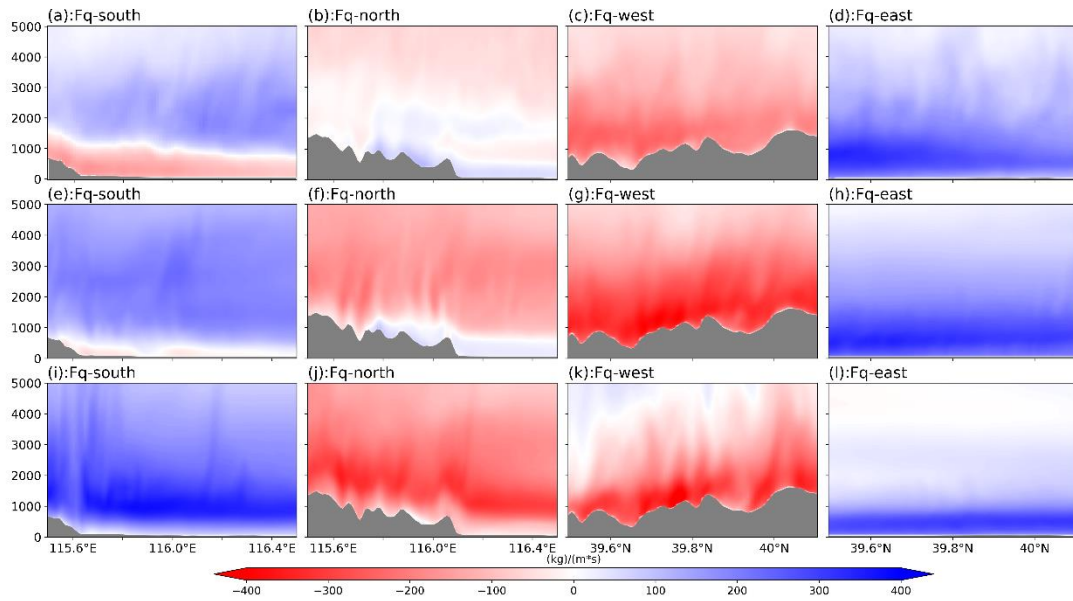
426  
 427  
 428  
 429  
 430  
 431  
 432  
 433  
 434

Figure 8 shows the magnitudes of the water vapor flux at the four boundaries of RegP for LU\_2020. An increase in net moisture convergence during each period leads to higher precipitable water over the region, which in turn provides more favorable conditions for precipitation. Specifically, the moisture inflow across the southern boundary (Figure 8(a), (e), (i)) and the eastern boundary (Figure 8(d), (h), (l)) represents meridional and zonal sources of water vapor entering the region. The outflow across the northern boundary (Figure 8(b), (f), (j)) and the western boundary (Figure 8(c), (g), (k)) reflects the moisture exported from the region. The difference

435 between the inflow and outflow moisture flux indicates net moisture income in each  
436 time period (shown in Table 4).

437 During period T1, about 49.58 kg/(m s) water vapor was transported southward  
438 at lower latitudinal levels along the southern boundary, while it was transported  
439 totally 58.63 kg/(m s) northward at high latitudes. As the Taihang Mountains extend  
440 in a southwest-northeast direction in the study area, the eastern zonal airflow was  
441 totally 130.50 kg/(m s), blocked by the Mountainous area and shifted southward  
442 which explained why water vapor was transported southward in northern boundary.  
443 Overall, the moisture input into the RegP was dominated by zonal water vapor  
444 transport. Although the meridional transport contributed a relatively large amount of  
445 moisture inflow, its substantial outflow resulted in a comparatively small net  
446 contribution to the regional moisture budget.

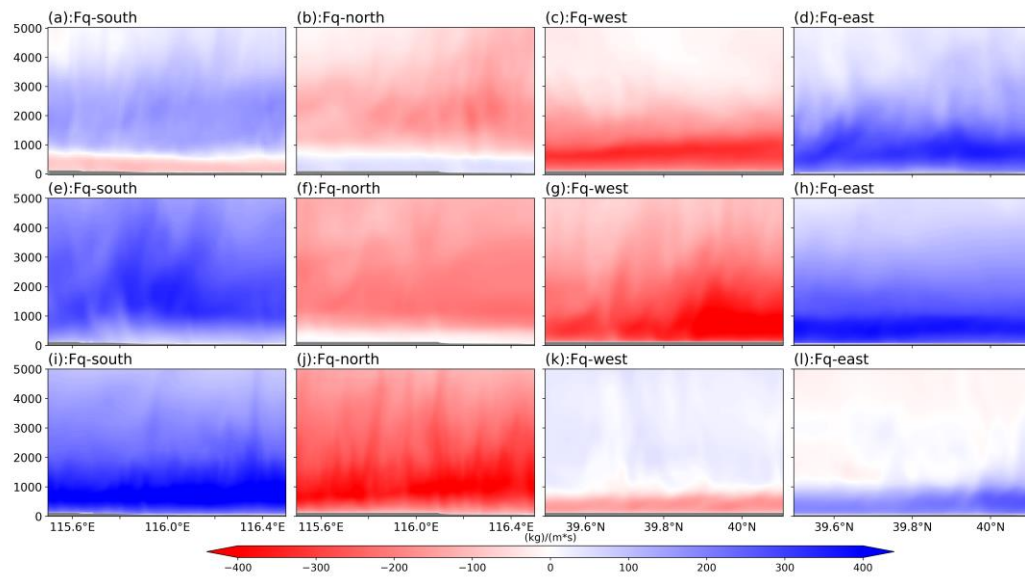
447 The water vapor flux distributions were similar during periods T2 and T3, while  
448 the magnitude of water vapor decreased from 23.58 kg/(m s) to 6.25 kg/(m s).  
449 Although the zonal water vapor transport increased to some extent, the total moisture  
450 inflow during the two periods remained comparable. Meridionally, the eastward water  
451 vapor flux decreased from -13.97 kg/(m s) to -23.71 kg/(m s). In addition, the water  
452 vapor transport during T3 became more concentrated in the lower layers which  
453 indicated the contribution of low-level water vapor transport to the precipitation  
454 process. Compared with that in T1, the northward water vapor flux at the southern  
455 boundary was significantly increased in T2 and T3. The northwestward transport  
456 increased and led to strong uplift motion in the mountainous area. Consequently, the  
457 mountainous areas may have been more prone to intense convective weather events  
458 due to the sufficient water vapor and air uplift during T2 and T3.



459  
 460 **Figure 8:** Distribution of water vapor flux magnitude in the LU\_2020 scheme across latitude-  
 461 height/longitude-height coordinates of RegP. Figures show the water vapor flux magnitude for  
 462 time periods T1 (a - d), T2 (e - h), and T3 (i - l), with fluxes from the south (a, e, i), north (b, f, j),  
 463 west (c, g, k), and east (d, h, l). Positive and negative water vapor flux values correspond to input  
 464 and output water vapor flux relative to RegP.

465

466 Orographic height significantly impacted water vapor flux transport, as shown by  
 467 the differences in the water vapor distribution between LU\_2020 (Figure 8) and  
 468 LU\_nohgt (Figure 9) and the corresponding water vapor flux transport in Table 4.  
 469 From a zonal perspective, orography considerably influenced the water vapor  
 470 distribution within RegP. Due to orographic effects, water vapor was lifted and its  
 471 northward transport was prevented, statistically reduced about 63.57 kg/(m s) in the  
 472 LU\_2020 (Figure 9 (a), (e), (i)), which also increased the total amount of zonal water  
 473 vapor flux in LU\_2020. From meridional perspective, the meridional water vapor flux  
 474 output from western boundary substantially decreased by 49.41 kg/(m s) and 79.38  
 475 kg/(m s) during the whole period, resulting in a noticeable rise in the water vapor  
 476 content in the entire region. Furthermore, the easterly winds were blocked and  
 477 diverted by the orographic effect of the mountains to the west of Beijing, which also  
 478 leads to a modest increase in the magnitude of the southward water vapor flux at the  
 479 southern boundary in the lower atmospheric layers.



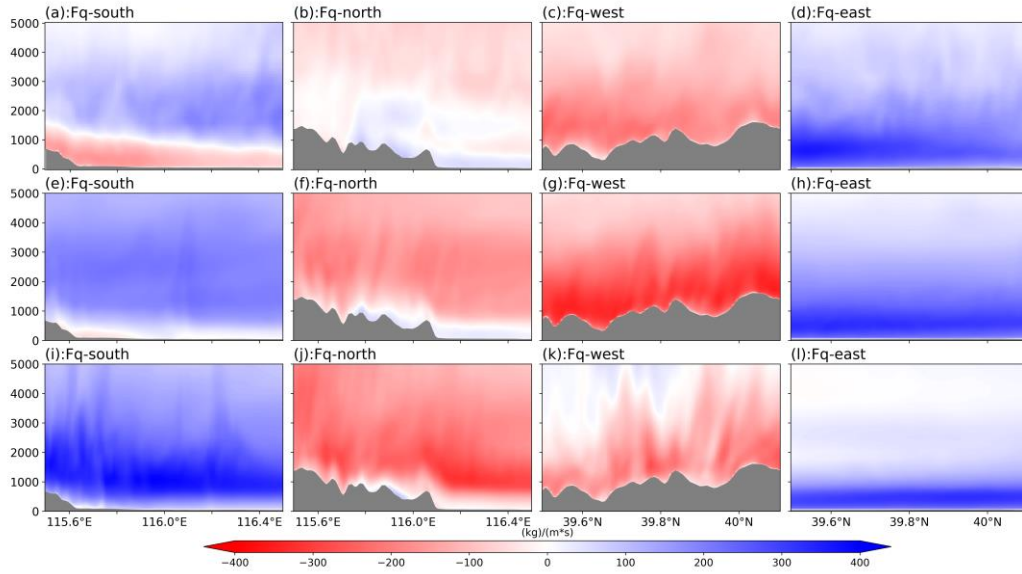
480

481 **Figure 9:** Water vapor fluxes as shown in Figure 8, where a - l depict the magnitude of the water  
 482 vapor flux from four directions in the LU\_nohgt scheme.

483

484 The impacts of the urbanization on water vapor transport are shown in Figure 10.

485 There was no significant difference between LU\_2020 and LU\_nourb in water vapor  
 486 flux during periods T1 and T2 as the difference between net convergence is smaller  
 487 than 10 kg/(m s). However, the differences mainly appeared at the western boundaries  
 488 of RegP during period T3. At the western boundary, the westward water vapor flux  
 489 was 30.98 kg/(m s) higher compared with that in LU\_nourb (Figure 10(k)). These  
 490 differences of moisture flux between different schemes were mainly due to wind  
 491 speed in lower troposphere. As urban land use can influence local atmospheric  
 492 circulation, such strong ascent induces horizontal convergence and a subsequent  
 493 conversion of horizontal momentum into vertical motion. Such momentum  
 494 redistribution can reduce the horizontal wind speed, particularly within the  
 495 convectively active region, leading to a reduction in moisture flux across the western  
 496 and northern boundaries.



497

498 **Figure 10:** Water vapor fluxes as shown in Figure 8, where a - l depict the magnitude of the water  
 499 vapor flux from four directions in the LU\_nourb scheme.

500

501

Table 4: The water vapor flux (kg/(m s)) during each period for different schemes.

	kg/(m s)	North	South	Zonal	West	East	Meridional	All
	LU_2020	58.63	-19.52	39.11	130.50	-100.61	29.89	69.00
T1	LU_nohgt	78.89	-83.09	-4.20	141.79	-110.93	30.86	26.66
	LU_nourb	55.42	-22.42	33.00	133.97	-94.19	39.78	72.78
	LU_2020	146.94	-109.39	37.55	146.05	-160.02	-13.97	23.58
T2	LU_nohgt	222.99	-146.99	76.00	176.09	-199.31	-23.22	52.78
	LU_nourb	152.31	-113.83	38.48	139.02	-150.29	-11.27	27.21
	LU_2020	199.32	-169.36	29.96	71.65	-95.36	-23.71	6.25
T3	LU_nohgt	228.22	-237.85	-9.63	32.12	-0.69	31.43	21.80
	LU_nourb	206.16	-160.40	45.76	74.65	-64.38	10.27	56.03

502

### 503 3.3.2. Differences in Near-surface Physical Variables

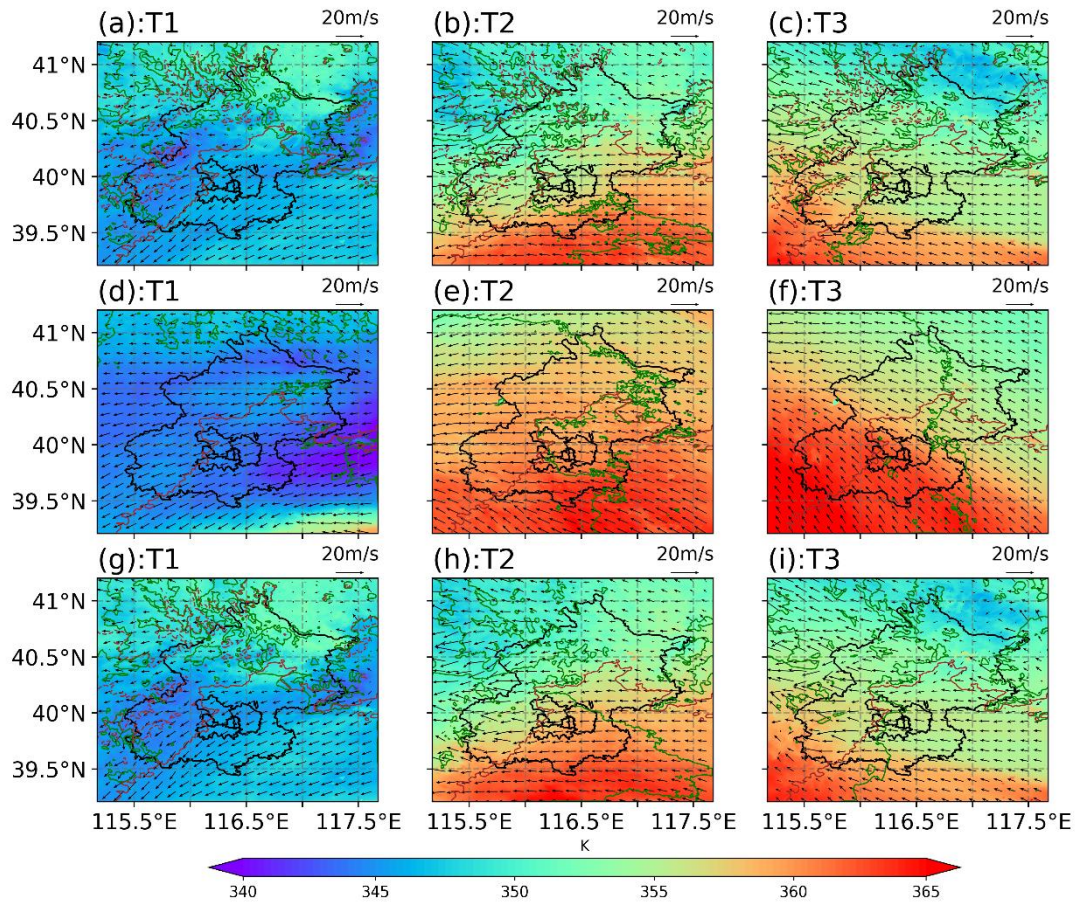
504 Near-surface physical quantities did not directly determine the magnitude of  
 505 precipitation, but the changes in the underlying surface were directly reflected in  
 506 variations in near-surface physical quantities, which then influenced the upper  
 507 atmosphere and subsequently affected the intensity of precipitation. Figure 11(a–c)  
 508 illustrates the horizontal distributions of the equivalent potential temperature, wind  
 509 speed, and the humidity during the three precipitation time periods.

510 During period T1 (Figure 11(a)), precipitation was mainly concentrated in the  
 511 southwestern mountainous and central region. The equivalent potential temperature  
 512 over Beijing remained between 346 and 347 K, but it was slightly lower than the

513 regional average in RegP. These results are consistent with the flux changes shown in  
514 Figure 7. The lowest equivalent potential temperature in Beijing was observed in the  
515 northwestern mountainous region (343 K). In addition, the 2-m relative humidity in  
516 Beijing during period T1 remained at an average value above 90%, and the 10-m  
517 wind direction was influenced by the circulation and orographic blocking, resulting in  
518 a northeastern wind. The wind direction was more erratic in the mountainous areas,  
519 where the relative humidity was slightly lower than that in the plains, and the  
520 precipitation was also relatively lower compared with the southern regions.

521 During period T2 (Figure 11 (b)), the precipitation entered the initial stage of the  
522 second precipitation phase, during which the precipitation mainly occurred in the  
523 southwestern mountainous areas. The warm and moist southerly air currents  
524 transported water vapor and also provided the energy required for precipitation. The  
525 equivalent potential temperature was higher in southern Beijing, and it decreased from  
526 south to north, a trend linked to the energy loss as the air moved northward. This  
527 variation was associated with the energy dissipation process as the airflow moved  
528 northward. The overall equivalent potential temperature gradually increased over time,  
529 from 351.6 K at 03:00 UTC on July 31 to 354.3 K at 06:00 UTC on July 31.

530 In period T3 (Figure 11(c)), the precipitation remained intense and the areas with  
531 the most intense precipitation were still located in the western mountainous areas of  
532 Beijing. The overall distribution of the equivalent potential temperature during this  
533 period was similar to that in period T2, and the highest values were still located in the  
534 southwestern mountainous areas of Beijing. The average equivalent potential  
535 temperature in Beijing remained within a range of 355K to 356 K. The overall relative  
536 humidity in the region was higher compared with that in period T2 (rising to 90.0%).  
537 The wind direction in the central urban area shifted slightly to the north due to the  
538 influence of the northerly air currents, but there was no significant change in the wind  
539 speed compared with that in period T2.



540  
 541 **Figure 11:** Simulated 2-m equivalent potential temperature, 2-m relative humidity, 10-m wind  
 542 speed, and orographic height for LU\_2020 scheme (a–c), LU\_nohgt scheme (d–f), and LU\_nourb  
 543 scheme (g–i). Three consecutive time periods were selected: T1 (a, d, g), T2 (b, e, h), and T3 (c, f,  
 544 i). In the figures, the 2-m temperature is represented by color-filled maps, areas with 2-m relative  
 545 humidity greater than 90% are outlined by green dashed lines, the 10-m wind speed is represented  
 546 by arrows, brown solid lines indicate orographic contours at 100 m, and brown dashed lines  
 547 represent orographic contours at 1000 m.

548

549 The effects of **orography** on the wind speed, temperature, and humidity were  
 550 evident (Figure 11(d–f)). During period T1, the equivalent potential temperature in the  
 551 LU\_2020 scheme over Beijing was significantly higher compared with that in the  
 552 LU\_nohgt scheme, **with** the largest increase observed in the eastern and northeastern  
 553 regions of Beijing. Due to the blocking effect of the mountains, the relative humidity  
 554 across the entire D04 area also increased during period T1. During periods T2 and T3,  
 555 the presence of the mountain range led to a notable decrease in the **equivalent**  
 556 potential temperature across the region compared with the LU\_nohgt scheme, mainly  
 557 due to the **transport** of water vapor along the Taihang Mountains to the Beijing area

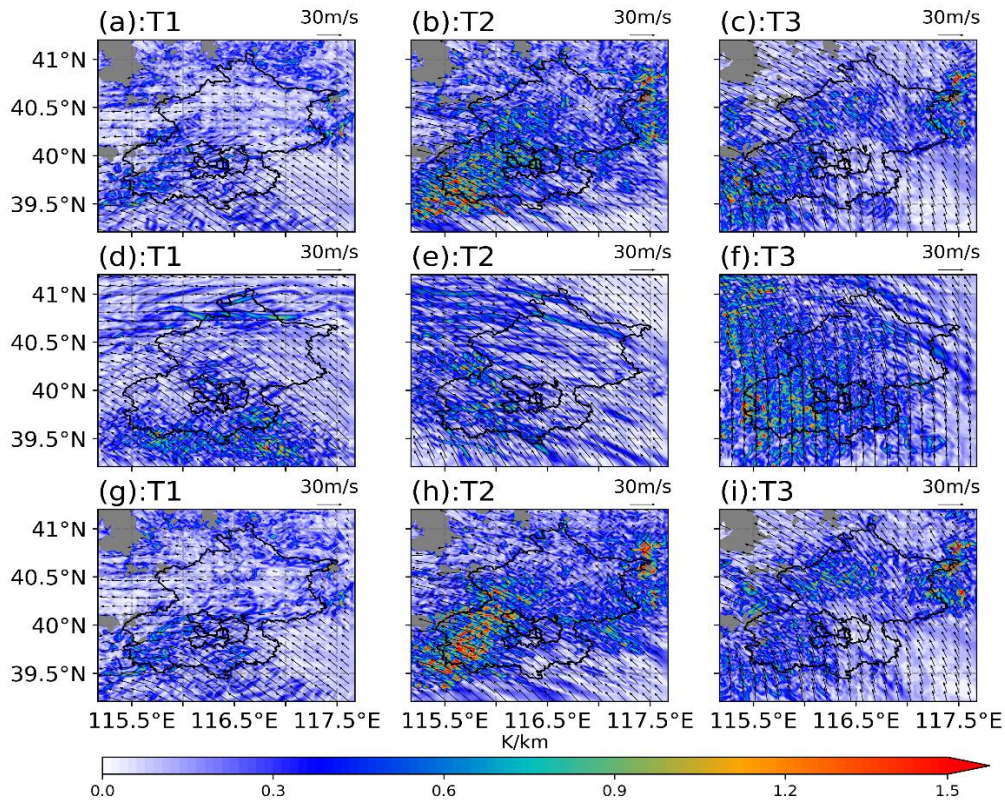
558 during the second stage, during which substantial amounts of water vapor and energy  
559 accumulated as the air mass passed through the mountains. The dissipation of energy  
560 and water vapor during this process led to significant reductions in the relative  
561 humidity and equivalent potential temperature in the plains and northern Beijing  
562 regions during these periods. Moreover, the presence of the western mountainous  
563 terrain led to the redistribution of the water vapor, resulting in significant variability  
564 in the humidity distribution in the mountainous areas. Minimal variation was found in  
565 the overall wind direction in the plains, and there were no significant differences  
566 between the two experimental groups across all three periods. However, in the  
567 mountainous areas, the orography induced air convergence at the boundary between  
568 the plains and mountains. Due to the complexity of the terrain, the wind speed and  
569 direction were more heterogeneous in the western mountainous areas.

570 The effects of urbanization were analyzed by comparing LU\_2020 (Figure 11(a–  
571 c)) and LU\_2020\_nourb (Figure 11(g–i)). The changes in precipitation were primarily  
572 concentrated in periods T2 and T3. During period T2, replacing urban underlying  
573 surfaces with croplands significantly altered the 2-m relative humidity in the central  
574 urban area, with an increase of more than 5%. This increase in the relative humidity  
575 led to greater accumulation of latent heat in the air, and the 2-m equivalent potential  
576 temperature in the central urban area increased by approximately 1 K as a result. The  
577 wind speed increased slightly in the urban area, with greater air convergence in the  
578 mountainous regions. During period T3, the increase in the relative humidity in the  
579 urban area was smaller compared with that in period T2 (increasing by around 3%).  
580 Wind convergence was still evident in the western mountainous regions. In particular,  
581 although the relative humidity in the central urban area increased significantly, there  
582 was no noticeable increase in the relative humidity in the downstream mountainous  
583 areas located to the east of the urban region.

584 Since presenting only the surface equivalent potential temperature could be  
585 insufficient to fully explain the influence mechanisms of the underlying surface, the  
586 gradient of equivalent potential temperature at representative times is further analyzed

587 to characterize the atmospheric stability (Figure 12). The orographic lifting exerts a  
588 significant modulation on the spatial distribution of the horizontal equivalent potential  
589 temperature gradient. During the T1 period, the LU\_nohgt scheme exhibits an  
590 eastward displacement of the maximum gradient compared with the LU\_2020,  
591 accompanied by a noticeable shift in the 850-hPa wind shear location. This indicates  
592 that, orographic lifting alters the low-level flow and thermodynamic structure, thereby  
593 modulates the distribution of moist baroclinicity and the position of the potential  
594 frontal zone. Therefore, it can provide a more favorable thermodynamic environment  
595 for convective development over the mountainous areas. During the T2 period,  
596 orographic lifting further enhances low-level moist baroclinicity and makes the high-  
597 gradient zone more continuous. Combined with the low-level wind shear, these  
598 conditions are conducive to frontogenetic processes and convective systems.

599 In contrast, although relatively large gradients still exist in the LU\_nohgt during  
600 the T3 period, the low-level convergence and vertical ascent are substantially  
601 weakened. It prevents the effective release of thermodynamic instability, and therefore  
602 the precipitation process consequently comes to an end. Meanwhile, the changes in  
603 urban land use also influence the precipitation intensity, especially during the T2  
604 period. The LU\_2020 scheme exhibits larger horizontal gradients over the  
605 southwestern mountainous region than LU\_nourb. This indicates that urbanization can  
606 enhance low-level moist baroclinicity in this area, which is favorable for  
607 strengthening frontal structures and increasing the likelihood of intense convection  
608 precipitation.



609

610 **Figure 12:** Gradient of equivalent potential temperature field for LU\_2020 scheme (a–c),  
 611 LU\_nohgt scheme (d–f), and LU\_nourb scheme (g–i) from 850 hPa. Three consecutive time  
 612 periods were selected: T1 (a, d, g), T2 (b, e, h), and T3 (c, f, i)

613

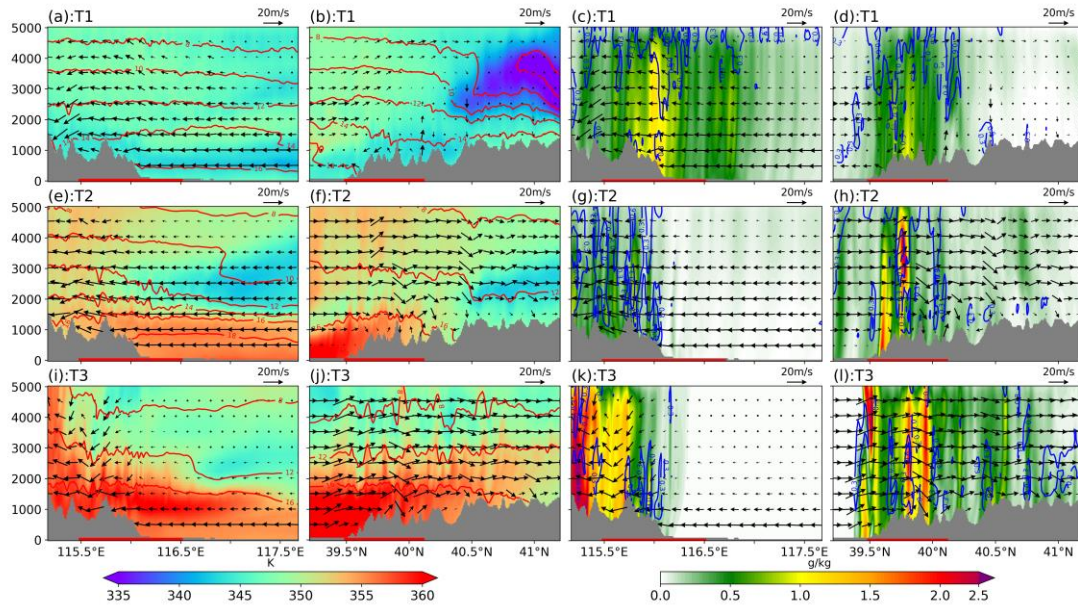
### 614 3.3.3. Differences in the Vertical Profile

615 Figure 13 presents the meridional and zonal vertical profiles for the three distinct  
 616 time periods. In the LU\_2020 scheme, convection was primarily confined to the  
 617 mountainous regions and the plains to the east of the mountains during period T1. The  
 618 orography blocking effect resulted in significant upward motion in both the  
 619 mountainous areas and adjacent plains. Around 02:00 on July 30, the eastward water  
 620 vapor flux was sufficiently high, leading to condensation of substantial amounts of  
 621 water vapor into cloud droplets and raindrops over the mountainous regions. The  
 622 latent heat released in this process induced fluctuations in the equivalent potential  
 623 temperature contours in the upper levels. In the zonal direction, cloud droplets and  
 624 raindrops were predominantly located over the southern mountains. In the northern  
 625 mountainous areas, due to the relatively low water vapor flux and lower equivalent  
 626 potential temperature, there was almost no vertical motion in the air, resulting in

627 negligible cloud droplet formation in this region.

628 During period T2, the atmosphere over the mountainous regions was  
629 characterized by vigorous convection in the meridional direction. In the southwestern  
630 mountains, higher equivalent potential temperatures correlated with greater cloud  
631 droplet concentrations. Both the southerly winds and vertical wind speeds increased  
632 significantly compared with those in period T1, and the cloud water and rainwater  
633 mixing ratios were elevated near 39.8°N. The cloud water mixing ratios were  
634 relatively high in other regions but this corresponded to the early stages of  
635 precipitation when cloud water had yet to fully transition into rainwater, resulting in  
636 low rainwater concentrations in most areas.

637 In the meridional direction, only the low-level wind speed over the plains was  
638 noticeably higher in period T3 compared with that in period T2. The low-level winds  
639 exhibited convergence, whereas the upper-level winds exhibited divergence in the  
640 southwestern mountainous region, and thus the equivalent potential temperature  
641 remained relatively high near the surface. In the zonal direction, notable convection  
642 occurred over the mountainous areas, accompanied by significant fluctuations in the  
643 near-surface equivalent potential temperature. In addition, the southward water vapor  
644 flux was relatively large during this period, and the energy, water vapor, and motion  
645 within the southwestern mountainous regions were conducive to the development of  
646 convection. As illustrated in Figure 13(i–k), both the cloud water and rainwater  
647 concentrations in the southwestern mountainous area increased compared with other  
648 regions. Consequently, the region experienced relatively higher precipitation during  
649 period T3.

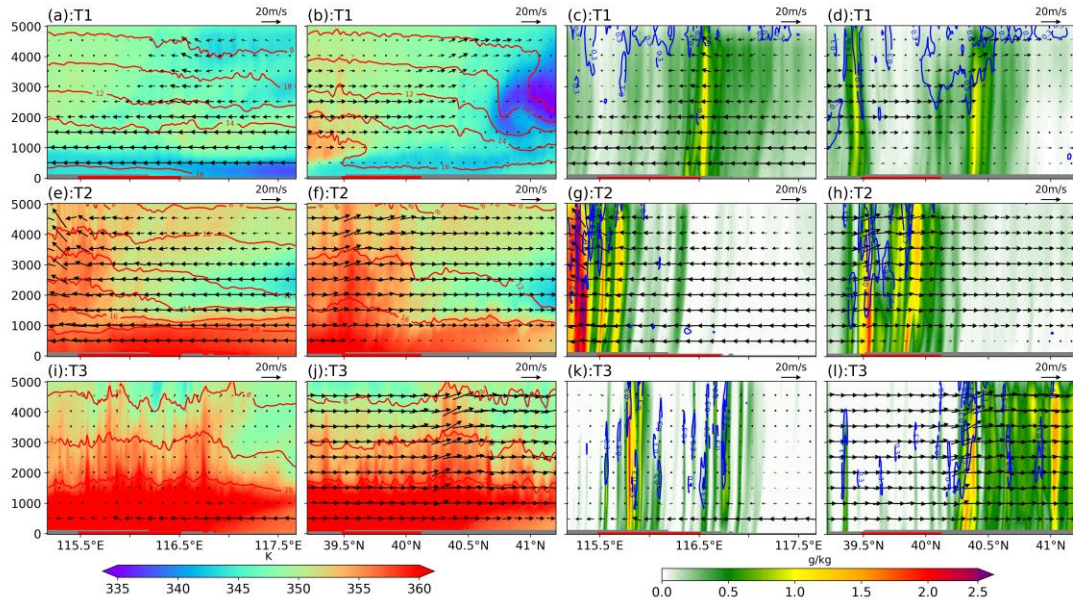


650  
 651 **Figure 13:** Meridional-vertical profiles (a, c, e, g, i, k) at 39.9°N and zonal-vertical profiles (b, d, f,  
 652 h, j, l) at 115.7°E for LU\_2020. In (a, b, e, f, i, j), the shaded areas represent the magnitude of the  
 653 equivalent potential temperature and red contours indicate the water vapor mixing ratio. In panels  
 654 (c, d, g, h, k, l), the shaded areas represent the rainwater mixing ratio and blue contours indicate  
 655 the cloud water mixing ratio. The arrows represent the horizontal wind vectors (with the vertical  
 656 wind speed amplified by a factor of five). Gray shading denotes the terrain height. The red line at  
 657 the bottom of the map indicates RegP, as shown in Figure 6.

658

659 Comparisons between the LU\_2020 (Figure 13) and LU\_nohgt (Figure 14)  
 660 experimental groups highlighted the convection observed during the three periods  
 661 driven by orographic uplift. In period T1, the uplift motion in the southern part of the  
 662 area facilitated the condensation of cloud droplets and raindrops, thus increasing the  
 663 precipitation intensity. In period T2, due to the higher equivalent potential temperature  
 664 and water vapor content of the atmosphere, strong convection persisted in the western  
 665 part of the study area in LU\_nohgt. The intensity of convection and water droplet  
 666 concentration in the atmosphere were markedly higher than those observed in the  
 667 LU\_2020 scheme. In the zonal direction, significant differences were observed  
 668 between the locations of cloud water droplet accumulation between the two  
 669 experimental setups. In period T3, convection shifted northward with the southerly  
 670 winds in the LU\_nohgt scheme. At the southern edge of the convective cloud mass,  
 671 the distributions of the wind speed, temperature, and humidity stabilized, indicating  
 672 the cessation of intense precipitation in the region. Despite the high energy levels

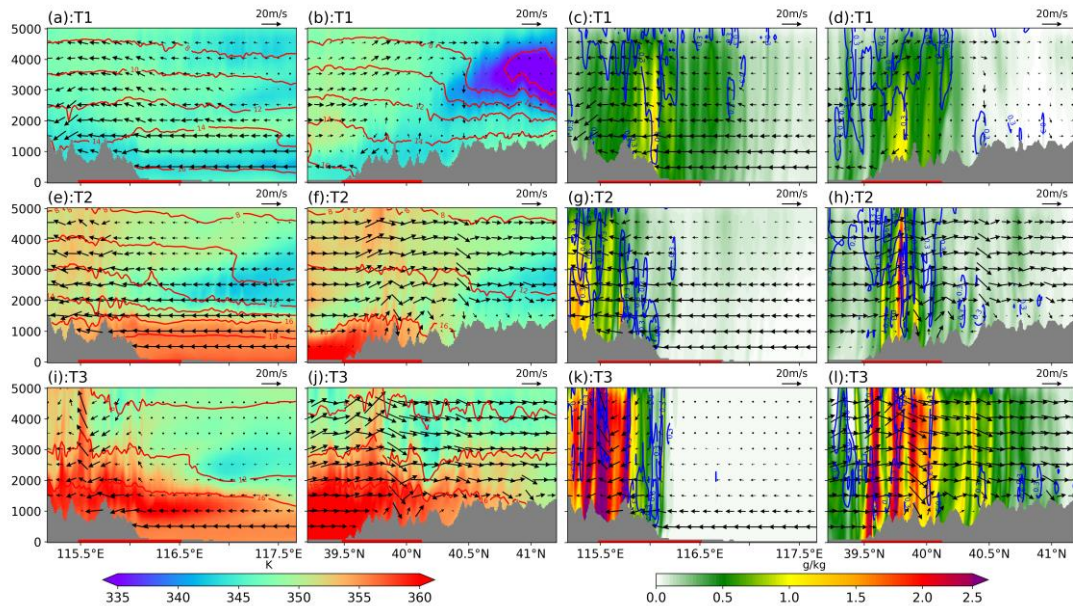
673 within the study area, the absence of orographic uplift led to a reduction in the  
 674 intensity of precipitation, and the precipitation event ended earlier compared with the  
 675 LU\_2020 scheme.



676  
 677 **Figure 14:** Meridional-vertical and zonal-vertical profiles for the LU\_nohgt schemes. The  
 678 physical quantities are consistent with those shown in Figure 12.  
 679

680 The impacts of urbanization on precipitation outcomes were examined by  
 681 comparing the LU\_2020 (Figure 13) and LU\_nourb (Figure 15) schemes, where the  
 682 primary effects were observed during periods T2 and T3. Due to the influence of  
 683 urbanization, there were no significant changes in the cloud water content over the  
 684 mountainous areas during period T2, besides the rainwater content was markedly  
 685 reduced, indicating a smaller amount of precipitation relative to LU\_nourb.  
 686 Urbanization led to decreases in the water vapor and energy transported into the  
 687 mountains from the eastern and southern parts of the region, thereby reducing the  
 688 condensation of cloud water and water vapor particles, which also agreed with the  
 689 delayed precipitation during T2 due to urbanization. During period T3, both the  
 690 meridional and zonal convection activities were weaker compared with LU\_nourb,  
 691 and the distribution of cloud droplet particles were also altered. The presence of the  
 692 city reduced the latent heat flux in the region, thereby diminishing the amount of  
 693 energy transported into the southwestern mountainous areas, and thus intense

694 precipitation occurred in the southwestern mountainous region during periods T2 to  
695 T3.



696 **Figure 15:** Meridional-vertical and zonal-vertical profiles for the LU\_nourb schemes. The  
697 physical quantities are consistent with those shown in Figure 12.  
698

699

## 700 4. Discussion

### 701 4.1 The intention of experiment design

702 In this study, simulations were conducted using the WRF model to investigate  
703 the changes in the timing and spatial distribution of precipitation during the “23 7”  
704 event caused by the effects of orography and urban land use. Previous studies have  
705 also analyzed the mechanisms related to precipitation and the impacts of orography on  
706 extreme precipitation events (Gao et al. 2024; Li et al. 2024b). In contrast to previous  
707 analyses, the effects of mountain-plain orographic conditions were explored by  
708 altering the underlying surfaces as well as investigating the impact of urbanization on  
709 this extreme precipitation event. The primary causes of this extreme precipitation  
710 event were identified by considering three time periods with significant differences in  
711 precipitation and analyzing the changes in basic physical quantities.

712 It has been pointed out that regional climate models have some limits on  
713 reproducing large-scale circulation features (Kukulies et al. 2023; Yu et al. 2024). To  
714 address this limitation, spectral nudging to the D01 domain was applied in all schemes.

715 The ERA5 reanalysis data was used to constrain large-scale circulation of the model,  
716 while allowing freely development for mesoscale and small-scale processes within the  
717 domain (Ma et al. 2022; Miguez-Macho et al. 2005; von Storch et al. 2000; Waldron  
718 et al. 1996). Therefore, it can provide a more accurate large-scale flow fields to the  
719 inner domains. The simulation results showed that, the orography and land use  
720 modifications in this study primarily influenced local circulation patterns and had  
721 limited **impacts** on synoptic-scale weather systems.

722

#### 723 4.2 Comparisons with related studies

724 According to previous research, the maximum reduction in precipitation due to  
725 urbanization during warm-season rainfall occurs in the northeastern region of Beijing  
726 (Song et al. 2014; Wang et al. 2018). However, in the present study, the largest  
727 reduction in precipitation induced by urbanization was observed in the southwestern  
728 mountainous region. **This difference is mainly caused by the different response**  
729 **patterns of mean and extreme precipitation events. The climatological statistics**  
730 **represent response of mean state, while extreme precipitation is often governed by**  
731 **nonlinear, specific dynamical forcing, and that may cause different distribution pattern**  
732 **(Liu and Niyogi 2019). As shown in the results, the water vapor transport of this**  
733 **precipitation event was mainly dominated by the southeasterly water vapor flux**  
734 **governed by the large-scale circulation, which thus triggered precipitation in the**  
735 **southwestern piedmont area of the Taihang Mountains. Although precipitation also**  
736 **occurred in the northwestern region, its intensity was weaker than that in the**  
737 **southwestern region, which is also the reason why this precipitation event is distinct**  
738 **from others.** Therefore, compared with the changes in the average distribution of  
739 seasonal precipitation in Beijing found in previous studies, individual case  
740 experiments may simulate precipitation distribution patterns that differ from the  
741 multi-year observed accumulated precipitation.

742 Previous studies also found that, the modifications of local urban land surface  
743 can influence local-scale atmospheric circulation (Kim et al. 2021; Sui et al. 2024;

744 Zajic et al. 2011). The widespread presence of impervious surfaces in urban areas  
745 restrained surface evaporation, by reducing the upward transport of moisture into the  
746 atmosphere. This process can lead to low relative humidity and reduce atmospheric  
747 instability, which in turn modifies the local precipitation distribution (Wang et al.  
748 2018). For the extreme precipitation event occurred on July 21 2012, the precipitation  
749 event was mostly generated by convective cells that were triggered by local orography  
750 and then propagated along a quasi-stationary linear convective system (Zhang et al.  
751 2013a). According to analyses of multiple extreme precipitation events in Beijing in  
752 recent years, urbanization can reduce rainfall in the urban area and increases rainfall  
753 downwind of the city. In some cases, the larger percentage of sealed area could give  
754 rise to the heavier precipitation or extreme rain events (Liu et al. 2021). As different  
755 types of precipitation or different weather conditions can lead to complex  
756 relationships between precipitation and elevation, even along the same slope (Gnann  
757 et al. 2025; Houze Jr. 2012). Therefore, urban effects of each event should be  
758 analyzed independently (Liu et al. 2021). This precipitation event is somewhat  
759 representative; however, for precipitation events under different initial conditions,  
760 further investigation is needed.

761

#### 762 4.3 Uncertainty in the experiment simulation

763 The choice of removing the terrain with an elevation above 100 meters was  
764 adopted in this study to ensure that the terrain in other regions would not be affected  
765 while eliminates the terrain of the Taihang and Yanshan Mountains. Similar  
766 experimental design had been used in other researches (Boos and Kuang 2010; Insel  
767 et al. 2010; Saurral et al. 2015; Song and Shao 2023). To detect the influence of the  
768 terrain removal operation, the experiment was repeated after removing all the terrain  
769 in the entire research area and the simulation of completely flat terrain was explored.  
770 It can be seen from Figure S5 that the spatial patterns of precipitation are similar for  
771 the schemes of 100 m and 0 m removal experiment. The center of maximum  
772 precipitation in 0 m removal experiment shifts eastward. This is mainly because the

773 flat terrain enhanced the northward transport of water vapor and further slowed the  
774 dissipation of the remnant low of Doksuri. It therefore increases the precipitable water  
775 over the region and leads to a more intense precipitation event. Statistically, the mean  
776 precipitation intensity is 4.2 mm/hr and 4.7 mm/hr for the 100 m and 0 m removal  
777 experiment, respectively. The RMSE and MAE of precipitation intensity is 1.54  
778 mm/hr and 1.17 mm/hr between these two schemes and the correlation coefficient is  
779 0.74. The results proved the strong relationships between the precipitations from 100  
780 m and 0 m removal experiment schemes, which may apply to other precipitation  
781 related variables.

782 The simulations were conducted using selected parameterization schemes and  
783 the impacts of the underlying surface were analyzed in this study. Physical  
784 parameterization schemes are widely recognized to exert substantial impacts on  
785 precipitation simulations, affecting not only intensity and duration, but also  
786 spatiotemporal distribution patterns. The parameterization method adopted in this  
787 study had also been used in other studies about urban extreme precipitation events  
788 (Luo et al. 2023; Ryu et al. 2016; Wang et al. 2018; Wang et al. 2023; Xian et al.  
789 2023), which can partly can prove the rationality of this study. Additional  
790 investigations into the parameterization schemes governing this precipitation event  
791 are required to elucidate the specific atmospheric conditions and physical mechanisms.  
792 Furthermore, due to constraints in data accessibility, only the 2020 MODIS land use  
793 dataset was obtained and used in our simulations, despite potential temporal  
794 mismatches with other input data periods. The Sentinel-2 satellite observations were  
795 further detected to assess the potential biases in land use between 2020 and 2023. The  
796 urban extent exhibited minimal variation between these years (Figure S6), validating  
797 the temporal stability of the MODIS baseline. However, the inherent differences in  
798 classification schemes between MODIS and Sentinel-2 precluded direct data  
799 integration or substitution. Therefore, the 2020 MODIS dataset was retained as the  
800 most recent consistent one, though it may introduce some uncertainties into the results.

801 Besides, the concentrations of aerosols emitted in urban areas could also have

802 influenced the extreme precipitation because it is largely driven by the coalescence of  
803 cloud droplets. Studies have shown that aerosols can lead to the formation of smaller-  
804 sized cloud droplets, increasing the effective radius of precipitation, and thus impact  
805 convective rainfall (Sun et al. 2022; Zhong et al. 2015). In addition, topographic  
806 variations can also affect the generation of cloud particles (Lee et al. 2018; Mazzetti et  
807 al. 2021). However, this study focuses on the impact of natural factors, particularly  
808 the underlying surface, on precipitation events. Aerosols are largely attributed to  
809 anthropogenic factors, therefore are not involved in this study and would be  
810 considered in future research.

811

## 812 **5. Conclusion**

813 In this study, the WRF model was used to analyze the extreme precipitation  
814 event that occurred in the Beijing region from July 29 to August 2, 2023. The effects  
815 of orography and land use on the precipitation process were evaluated by removing  
816 the orography and replacing urban land use types with croplands from the updated  
817 land use experiment group. The results showed that, the areas influenced most  
818 significantly by orography were concentrated in the southwestern mountainous region  
819 of Beijing. Presence of terrain caused orographic uplift and increased the precipitation  
820 within the mountainous area by more than 40% during the event. This main because  
821 that the mountainous area blocked the existence of the low-pressure system of  
822 typhoon Doksuri from propagating northward and lead to extended duration of the  
823 precipitation event by approximately 12 h. The underlying urban surfaces also altered  
824 the overall precipitation process. For the scheme removing the underlying urban  
825 surfaces the enhanced water vapor flux transported by low-level easterly winds to the  
826 southwestern mountainous region of the city increased the accumulation of energy  
827 and water vapor in the region. After July 31, the accumulation of sufficient energy and  
828 moisture in the southwestern mountainous region strengthened the intensity of  
829 precipitation. In addition, removing the underlying urban surface caused an increase  
830 in the wind speed in the plain areas, which led to large convergence at the mountain

831 boundary and contributed to stronger precipitation. These findings can help us with  
832 the prevention and response to similar future events, and possibly reduce the  
833 likelihood of disasters.

834

### 835 **Financial Support**

836 This study was funded by the National Natural Science Foundation of China  
837 (42077421 and 41930970).

838

### 839 **Data Availability Statement**

840 The ERA5 reanalysis data can be downloaded at Climate Data Store  
841 (<https://cds.climate.copernicus.eu>). The gauge observations were from the China  
842 Meteorological Administration (version 2.0; <http://data.cma.cn/en>). The CMOPRH  
843 precipitation data were obtained from Climate Prediction Center.  
844 (<https://www.ncei.noaa.gov/products/climate-data-records/precipitation-cmorph>). The  
845 updated land use/land cover data from MCD12Q1 V6 over Beijing region are  
846 available from the Land Processes Distributed Active Archive Center  
847 (<https://lpdaac.usgs.gov/>).

848

### 849 **Author Contributions**

850 **HC**: Conceptualization; formal analysis; methodology; software; validation;  
851 visualization; writing – original draft; writing – review and editing. **HY**:  
852 Conceptualization; methodology; writing – review and editing. **XZ**: methodology;  
853 writing – review and editing. **GW**: Conceptualization; data curation; funding  
854 acquisition; investigation resources; supervision; writing – original draft; writing –  
855 review and editing.

856

### 857 **Conflicts of Interest**

858 The authors declare that they have no conflict of interest.

859

860 **References**

- 861 Ayat, H., J. P. Evans, S. C. Sherwood, and J. Soderholm, 2022: Intensification of subhourly heavy  
862 rainfall. *Science*, 378, 655-+.
- 863 Bhattarai, S., and R. Talchabhadel, 2024: Comparative Analysis of Satellite -Based Precipitation  
864 Data across the CONUS and Hawaii: Identifying Optimal Satellite Performance. *Remote*  
865 *Sensing*, 16, 3058.
- 866 Boos, W. R., and Z. Kuang, 2010: Dominant control of the South Asian monsoon by orographic  
867 insulation versus plateau heating. *Nature*, 463, 218-222.
- 868 Bornstein, R., and Q. L. Lin, 2000: Urban heat islands and summertime convective thunderstorms  
869 in Atlanta: three case studies. *Atmospheric Environment*, 34, 507-516.
- 870 Chen, F., and J. Dudhia, 2001: Coupling an advanced land surface-hydrology model with the  
871 Penn State-NCAR MM5 modeling system. Part II: Preliminary model validation. *Monthly*  
872 *Weather Review*, 129, 587-604.
- 873 Chen, F., H. Kusaka, R. Bornstein, J. Ching, C. S. B. Grimmond, S. Grossman-Clarke, T. Loridan, K.  
874 W. Manning, A. Martilli, S. G. Miao, D. Sailor, F. P. Salamanca, H. Taha, M. Tewari, X. M.  
875 Wang, A. A. Wyszogrodzki, and C. L. Zhang, 2011: The integrated WRF/urban modelling  
876 system: development, evaluation, and applications to urban environmental problems.  
877 *International Journal of Climatology*, 31, 273-288.
- 878 Chen, M. X., Y. C. Wang, F. Gao, and X. Xiao, 2014: Diurnal evolution and distribution of warm-  
879 season convective storms in different prevailing wind regimes over contiguous North  
880 China. *Journal of Geophysical Research-Atmospheres*, 119, 2742-2763.
- 881 Cornejo, I. C., A. K. Rowel, K. L. Rasmussen, and J. C. Dehartb, 2024: Orographic Controls on  
882 Extreme Precipitation Associated with a Mei-Yu Front. *Monthly Weather Review*, 152,  
883 531-551.
- 884 Dai, P. X., J. Nie, Y. Yu, and R. G. Wu, 2024: Constraints on regional projections of mean and  
885 extreme precipitation under warming. *Proceedings of the National Academy of Sciences*  
886 *of the United States of America*, 121.
- 887 Davolio, S., A. Buzzi, and P. Malguzzi, 2009: Orographic triggering of long lived convection in  
888 three dimensions. *Meteorology and Atmospheric Physics*, 103, 35-44.
- 889 Dixon, P. G., and T. L. Mote, 2003: Patterns and causes of Atlanta's urban heat island-initiated  
890 precipitation. *Journal of Applied Meteorology*, 42, 1273-1284.
- 891 Dou, J. J., Y. C. Wang, R. Bornstein, and S. G. Miao, 2015: Observed Spatial Characteristics of  
892 Beijing Urban Climate Impacts on Summer Thunderstorms. *Journal of Applied*  
893 *Meteorology and Climatology*, 54, 94-105.
- 894 Du, Y., G. X. Chen, B. Han, L. Q. Bai, and M. H. Li, 2020: Convection Initiation and Growth at the  
895 Coast of South China. Part II: Effects of the Terrain, Coastline, and Cold Pools. *Monthly*  
896 *Weather Review*, 148, 3871-3892.
- 897 Dudhia, J., 1989: Numerical Study of Convection Observed during the Winter Monsoon  
898 Experiment Using a Mesoscale Two-Dimensional Model. *Journal of the Atmospheric*  
899 *Sciences*, 46, 3077-3107.
- 900 Ebert, E. E., J. E. Janowiak, and C. Kidd, 2007: Comparison of near-real-time precipitation  
901 estimates from satellite observations and numerical models. *Bulletin of the American*  
902 *Meteorological Society*, 88, 47-64.
- 903 Freitag, B. M., U. S. Nair, and D. Niyogi, 2018: Urban Modification of Convection and Rainfall in

904 Complex Terrain. *Geophysical Research Letters*, 45, 2507-2515.

905 Friedl, M., D. Sulla-Menashe, 2019: MCD12Q1 MODIS/Terra+Aqua Land Cover Type Yearly L3  
906 Global 500m SIN Grid V006. NASA EOSDIS Land Processes Distributed Active Archive  
907 Center.

908 Fu, Y. Y., S. J. Jiang, Y. N. Mao, and G. C. Wu, 2024: Urbanization reshapes extreme precipitation  
909 metrics in typical urban agglomerations of Eastern China. *Atmospheric Research*, 300.

910 Gao, X. Y., J. S. Sun, J. F. Yin, A. Abulikemu, C. Wu, X. D. Liang, and R. D. Xia, 2024: The impact of  
911 mountain-plain thermal contrast on precipitation distributions during the "23.7" record-  
912 breaking heavy rainfall over North China. *Atmospheric Research*, 310.

913 Gao, Z. B., J. S. Zhu, Y. Guo, N. Luo, Y. Fu, and T. T. Wang, 2021: Impact of Land Surface  
914 Processes on a Record-Breaking Rainfall Event on May 06-07, 2017, in Guangzhou,  
915 China. *Journal of Geophysical Research-Atmospheres*, 126.

916 Gimeno, L., A. Drumond, R. Nieto, R. M. Trigo, and A. Stohl, 2010: On the origin of continental  
917 precipitation. *Geophysical Research Letters*, 37.

918 Gnann, S., J. W. Baldwin, M. O. Cuthbert, T. Gleeson, W. Schwanghart, and T. Wagener, 2025: The  
919 Influence of Topography on the Global Terrestrial Water Cycle. *Reviews of Geophysics*,  
920 63, e2023RG000810.

921 Gómez, B., and G. Miguez-Macho, 2017: The impact of wave number selection and spin-up time  
922 in spectral nudging. *Quarterly Journal of the Royal Meteorological Society*, 143, 1772-  
923 1786.

924 He, H. Z., and F. Q. Zhang, 2010: Diurnal Variations of Warm-Season Precipitation over Northern  
925 China. *Monthly Weather Review*, 138, 1017-1025.

926 He, Y., J. Wang, and J. Feng, 2023: A Typical Weakly Forced Mountain-To-Plain Extreme  
927 Precipitation Event Exacerbated by Urbanization in Beijing. *Journal of Geophysical  
928 Research: Atmospheres*, 128, e2023JD039275.

929 Hersbach, H., B. Bell, P. Berrisford, S. Hirahara, A. Horányi, J. Muñoz-Sabater, J. Nicolas, C.  
930 Peubey, R. Radu, D. Schepers, A. Simmons, C. Soci, S. Abdalla, X. Abellan, G. Balsamo, P.  
931 Bechtold, G. Biavati, J. Bidlot, M. Bonavita, G. De Chiara, P. Dahlgren, D. Dee, M.  
932 Diamantakis, R. Dragani, J. Flemming, R. Forbes, M. Fuentes, A. Geer, L. Haimberger, S.  
933 Healy, R. J. Hogan, E. Hólm, M. Janisková, S. Keeley, P. Laloyaux, P. Lopez, C. Lupu, G.  
934 Radnoti, P. de Rosnay, I. Rozum, F. Vamborg, S. Villaume, and J.-N. Thépaut, 2020a: The  
935 ERA5 global reanalysis. *Quarterly Journal of the Royal Meteorological Society*, 146,  
936 1999-2049.

937 Hersbach, H., B. Bell, P. Berrisford, S. Hirahara, A. Horányi, J. Muñoz-Sabater, J. Nicolas, C.  
938 Peubey, R. Radu, D. Schepers, A. Simmons, C. Soci, S. Abdalla, X. Abellan, G. Balsamo, P.  
939 Bechtold, G. Biavati, J. Bidlot, M. Bonavita, G. De Chiara, P. Dahlgren, D. Dee, M.  
940 Diamantakis, R. Dragani, J. Flemming, R. Forbes, M. Fuentes, A. Geer, L. Haimberger, S.  
941 Healy, R. J. Hogan, E. Hólm, M. Janisková, S. Keeley, P. Laloyaux, P. Lopez, C. Lupu, G.  
942 Radnoti, P. de Rosnay, I. Rozum, F. Vamborg, S. Villaume, and J. N. Thépaut, 2020b: The  
943 ERA5 global reanalysis. *Quarterly Journal of the Royal Meteorological Society*, 146,  
944 1999-2049.

945 Hjelmfelt, M. R., 1982: Numerical Simulation of the Effects of St. Louis on Mesoscale Boundary-  
946 Layer Airflow and Vertical Air Motion: Simulations of Urban vs Non-Urban Effects.  
947 *Journal of Applied Meteorology*, 21, 1239-1257.

948 Holst, C. C., C.-Y. Tam, and J. C. L. Chan, 2016: Sensitivity of urban rainfall to anthropogenic heat  
949 flux: A numerical experiment. *Geophysical Research Letters*, 43, 2240-2248.

950 Hong, S. Y., Y. Noh, and J. Dudhia, 2006: A new vertical diffusion package with an explicit  
951 treatment of entrainment processes. *Monthly Weather Review*, 134, 2318-2341.

952 Hong, S. Y., and J.-O. J. Lim, 2006: The WRF single-moment 6-class microphysics scheme  
953 (WSM6). *Journal of the Korean Meteorological Society*, 42, 129-151.

954 Houze Jr., R. A., 2012: Orographic effects on precipitating clouds. *Reviews of Geophysics*, 50.

955 Huang, Y. J., Y. B. Liu, Y. W. Liu, H. Y. Li, and J. C. Kniviel, 2019: Mechanisms for a Record-  
956 Breaking Rainfall in the Coastal Metropolitan City of Guangzhou, China: Observation  
957 Analysis and Nested Very Large Eddy Simulation With the WRF Model. *Journal of*  
958 *Geophysical Research-Atmospheres*, 124, 1370-1391.

959 Insel, N., C. J. Poulsen, and T. A. Ehlers, 2010: Influence of the Andes Mountains on South  
960 American moisture transport, convection, and precipitation. *Climate Dynamics*, 35,  
961 1477-1492.

962 Janjić, Z. I., 1994: The Step-Mountain Eta Coordinate Model: Further Developments of the  
963 Convection, Viscous Sublayer, and Turbulence Closure Schemes. *Monthly Weather*  
964 *Review*, 122, 927-945.

965 Jauregui, E., and E. Romales, 1996: Urban effects on convective precipitation in Mexico city.  
966 *Atmospheric Environment*, 30, 3383-3389.

967 Jiang, S.-h., M. Zhou, L.-l. Ren, X.-r. Cheng, and P.-j. Zhang, 2016: Evaluation of latest TMPA and  
968 CMORPH satellite precipitation products over Yellow River Basin. *Water Science and*  
969 *Engineering*, 9, 87-96.

970 Joyce, R. J., J. E. Janowiak, P. A. Arkin, and P. P. Xie, 2004: CMORPH: A method that produces  
971 global precipitation estimates from passive microwave and infrared data at high spatial  
972 and temporal resolution. *Journal of Hydrometeorology*, 5, 487-503.

973 Kain, J. S., 2004: The Kain-Fritsch convective parameterization: An update. *Journal of Applied*  
974 *Meteorology*, 43, 170-181.

975 Kim, G., J. Lee, M.-l. Lee, and D. Kim, 2021: Impacts of urbanization on atmospheric circulation  
976 and aerosol transport in a coastal environment simulated by the WRF-Chem coupled  
977 with urban canopy model. *Atmospheric Environment*, 249, 118253.

978 Kukulies, J., A. F. Prein, J. Curio, H. Yu, and D. Chen, 2023: Kilometer-Scale Multimodel and  
979 Multiphysics Ensemble Simulations of a Mesoscale Convective System in the Lee of the  
980 Tibetan Plateau: Implications for Climate Simulations. *Journal of Climate*, 36, 5963-5987.

981 Lee, J. T., K. Y. Ko, D. I. Lee, C. H. You, and Y. C. Liou, 2018: Enhancement of orographic  
982 precipitation in Jeju Island during the passage of Typhoon Khanun (2012). *Atmospheric*  
983 *Research*, 201, 58-71.

984 Li, S., Y. N. Chen, W. Wei, G. H. Fang, and W. L. Duan, 2024a: The increase in extreme  
985 precipitation and its proportion over global land. *Journal of Hydrology*, 628.

986 Li, W. B., S. Chen, G. X. Chen, W. M. Sha, C. Luo, Y. R. Feng, Z. P. Wen, and B. M. Wang, 2011:  
987 Urbanization signatures in strong versus weak precipitation over the Pearl River Delta  
988 metropolitan regions of China. *Environmental Research Letters*, 6.

989 Li, X., S. Zhao, and D. Wang, 2024b: Roles of synoptic characteristics and microphysics processes  
990 on the heavy rain event over Beijing region during 29 July to 2 August 2023. *Frontiers in*  
991 *Earth Science*, Volume 12 - 2024.

992 Li, X., S. W. Zhao, and D. H. Wang, 2024c: Roles of synoptic characteristics and microphysics  
993 processes on the heavy rain event over Beijing region during 29 July to 2 August 2023.  
994 *Frontiers in Earth Science*, 12.

995 Liang, P., and Y. H. Ding, 2017: The Long-term Variation of Extreme Heavy Precipitation and Its  
996 Link to Urbanization Effects in Shanghai during 1916-2014. *Advances in Atmospheric*  
997 *Sciences*, 34, 321-334.

998 Lin, Y. L., S. Chiao, T. A. Wang, M. L. Kaplan, and R. P. Weglarz, 2001: Some common ingredients  
999 for heavy orographic rainfall. *Weather and Forecasting*, 16, 633-660.

1000 Liu, J., and D. Niyogi, 2019: Meta-analysis of urbanization impact on rainfall modification.  
1001 *Scientific Reports*, 9, 7301.

1002 Liu, J., K. H. Schlünzen, T. Frisius, and Z. Tian, 2021: Effects of urbanization on precipitation in  
1003 Beijing. *Physics and Chemistry of the Earth, Parts A/B/C*, 122, 103005.

1004 Liu, P., A. P. Tsimpidi, Y. Hu, B. Stone, A. G. Russell, and A. Nenes, 2012: Differences between  
1005 downscaling with spectral and grid nudging using WRF. *Atmos. Chem. Phys.*, 12, 3601-  
1006 3610.

1007 Liu, S., J. Wang, and H. Wang, 2022: Assessing 10 Satellite Precipitation Products in Capturing the  
1008 July 2021 Extreme Heavy Rain in Henan, China. *Journal of Meteorological Research*, 36,  
1009 798-808.

1010 Luo, Y., J. Zhang, M. Yu, X. Liang, R. Xia, Y. Gao, X. Gao, and J. Yin, 2023: On the Influences of  
1011 Urbanization on the Extreme Rainfall over Zhengzhou on 20 July 2021: A Convection-  
1012 Permitting Ensemble Modeling Study. *Advances in Atmospheric Sciences*, 40, 393-409.

1013 Ma, M., P. Hui, D. Liu, P. Zhou, and J. Tang, 2022: Convection-permitting regional climate  
1014 simulations over Tibetan Plateau: re-initialization versus spectral nudging. *Climate*  
1015 *Dynamics*, 58, 1719-1735.

1016 Ma, Y., Y. Yang, X. Mai, C. Qiu, X. Long, and C. Wang, 2016: Comparison of Analysis and Spectral  
1017 Nudging Techniques for Dynamical Downscaling with the WRF Model over China.  
1018 *Advances in Meteorology*, 2016, 4761513.

1019 Mahoney, K. M., 2016: The Representation of Cumulus Convection in High-Resolution  
1020 Simulations of the 2013 Colorado Front Range Flood. *Monthly Weather Review*, 144,  
1021 4265-4278.

1022 Mazzetti, T. O., B. Geerts, L. L. Xue, S. Tessorf, C. Weeks, and Y. G. Wang, 2021: Potential for  
1023 Ground-Based Glaciogenic Cloud Seeding over Mountains in the Interior Western  
1024 United States and Anticipated Changes in a Warmer Climate. *Journal of Applied*  
1025 *Meteorology and Climatology*, 60, 1245-1263.

1026 Miguez-Macho, G., G. L. Stenchikov, and A. Robock, 2004: Spectral nudging to eliminate the  
1027 effects of domain position and geometry in regional climate model simulations. *Journal*  
1028 *of Geophysical Research-Atmospheres*, 109.

1029 Miguez-Macho, G., G. L. Stenchikov, and A. Robock, 2005: Regional Climate Simulations over  
1030 North America: Interaction of Local Processes with Improved Large-Scale Flow. *Journal*  
1031 *of Climate*, 18, 1227-1246.

1032 Mlawer, E. J., S. J. Taubman, P. D. Brown, M. J. Iacono, and S. A. Clough, 1997: Radiative transfer  
1033 for inhomogeneous atmospheres: RRTM, a validated correlated-k model for the  
1034 longwave. *Journal of Geophysical Research-Atmospheres*, 102, 16663-16682.

1035 Nicolas, Q., and W. R. Boos, 2024: Understanding the Spatiotemporal Variability of Tropical

1036 Orographic Rainfall Using Convective Plume Buoyancy. *Journal of Climate*, 37, 1737-  
1037 1757.

1038 Nie, W. S., B. F. Zaitchik, G. H. Ni, and T. Sun, 2017: Impacts of Anthropogenic Heat on  
1039 Summertime Rainfall in Beijing. *Journal of Hydrometeorology*, 18, 693-712.

1040 Niyogi, D., P. Pyle, M. Lei, S. P. Arya, C. M. Kishtawal, M. Shepherd, F. Chen, and B. Wolfe, 2011:  
1041 Urban Modification of Thunderstorms: An Observational Storm Climatology and Model  
1042 Case Study for the Indianapolis Urban Region. *Journal of Applied Meteorology and  
1043 Climatology*, 50, 1129-1144.

1044 Oke, T. R., 1982: The energetic basis of the urban heat island. *Quarterly Journal of the Royal  
1045 Meteorological Society*, 108, 1-24.

1046 Pei, L., S.-G. Miao, X.-Y. Huang, Z.-W. Yan, and D. Chen, 2025: Assessing the added value of  
1047 convection-permitting modeling for urban climate research: A case study in eastern  
1048 China. *Advances in Climate Change Research*, 16, 1-11.

1049 Pendergrass, A. G., and R. Knutti, 2018: The Uneven Nature of Daily Precipitation and Its Change.  
1050 *Geophysical Research Letters*, 45, 11980-11988.

1051 Ryu, Y.-H., J. A. Smith, E. Bou-Zeid, and M. L. Baeck, 2016: The Influence of Land Surface  
1052 Heterogeneities on Heavy Convective Rainfall in the Baltimore–Washington  
1053 Metropolitan Area. *Monthly Weather Review*, 144, 553-573.

1054 Saurral, R. I., I. A. Camilloni, and T. Ambrizzi, 2015: Links between topography, moisture fluxes  
1055 pathways and precipitation over South America. *Climate Dynamics*, 45, 777-789.

1056 Skamarock, W. C., J. B. Klemp, J. Dudhia, D. O. Gill, Z. Liu, J. Berner, W. Wang, J. G. Powers, M. G.  
1057 Duda, D. M. Barker, and X.-Y. Huang, 2019: A Description of the Advanced Research  
1058 WRF Version 4. NCAR Tech. Note NCAR/TN-556+STR, 145 pp.

1059 Smith, R. B., 2006: Progress on the theory of orographic precipitation. *Tectonics, Climate, and  
1060 Landscape Evolution*, 1-16.

1061 Song, X. M., J. Y. Zhang, A. AghaKouchak, S. Sen Roy, Y. Q. Xuan, G. Q. Wang, R. M. He, X. J.  
1062 Wang, and C. S. Liu, 2014: Rapid urbanization and changes in spatiotemporal  
1063 characteristics of precipitation in Beijing metropolitan area. *Journal of Geophysical  
1064 Research-Atmospheres*, 119, 11250-11271.

1065 Song, Y., and M. Shao, 2023: Impacts of Complex Terrain Features on Local Wind Field and  
1066 PM2.5 Concentration. *Atmosphere*, 761.

1067 Spero, T. L., M. J. Otte, J. H. Bowden, and C. G. Nolte, 2014: Improving the representation of  
1068 clouds, radiation, and precipitation using spectral nudging in the Weather Research and  
1069 Forecasting model. *Journal of Geophysical Research-Atmospheres*, 119, 11682-11694.

1070 Sui, X., Z.-L. Yang, M. Shepherd, and D. Niyogi, 2024: Global scale assessment of urban  
1071 precipitation anomalies. *Proceedings of the National Academy of Sciences*, 121,  
1072 e2311496121.

1073 Sun, N., Y. F. Fu, L. Zhong, and R. Li, 2022: Aerosol effects on the vertical structure of  
1074 precipitation in East China. *NPJ Climate and Atmospheric Science*, 5.

1075 Sun, Q., X. Zhang, F. Zwiers, S. Westra, and L. V. Alexander, 2021: A Global, Continental, and  
1076 Regional Analysis of Changes in Extreme Precipitation. *Journal of Climate*, 34, 243-258.

1077 Sun, R., H. Yuan, X. Liu, and X. Jiang, 2016: Evaluation of the latest satellite–gauge precipitation  
1078 products and their hydrologic applications over the Huaihe River basin. *Journal of  
1079 Hydrology*, 536, 302-319.

1080 Tewari, M., F. Chen, J. Dudhia, P. Ray, S. G. Miao, E. Nikolopoulos, and L. Treinish, 2022:  
1081 Understanding the sensitivity of WRF hindcast of Beijing extreme rainfall of 21 July 2012  
1082 to microphysics and model initial time. *Atmospheric Research*, 271.

1083 Trenberth, K. E., A. Dai, R. M. Rasmussen, and D. B. Parsons, 2003: The changing character of  
1084 precipitation. *Bulletin of the American Meteorological Society*, 84, 1205-1217.

1085 von Storch, H., H. Langenberg, and F. Feser, 2000: A spectral nudging technique for dynamical  
1086 downscaling purposes. *Monthly Weather Review*, 128, 3664-3673.

1087 Waldron, K. M., J. Paegle, and J. D. Horel, 1996: Sensitivity of a Spectrally Filtered and Nudged  
1088 Limited-Area Model to Outer Model Options. *Monthly Weather Review*, 124, 529-547.

1089 Wang, J., J. M. Feng, and Z. W. Yan, 2015: Potential sensitivity of warm season precipitation to  
1090 urbanization extents: Modeling study in Beijing-Tianjin-Hebei urban agglomeration in  
1091 China. *Journal of Geophysical Research-Atmospheres*, 120, 9408-9425.

1092 Wang, J., J. Feng, and Z. Yan, 2018: Impact of Extensive Urbanization on Summertime Rainfall in  
1093 the Beijing Region and the Role of Local Precipitation Recycling. *Journal of Geophysical  
1094 Research: Atmospheres*, 123, 3323-3340.

1095 Wang, J., S. Miao, Q.-V. Doan, F. Chen, R. Abolafia-Rosenzweig, L. Yang, G. Zhang, Y. Zhang, J.  
1096 Dou, and Y. Xu, 2023: Quantifying the Impacts of High-Resolution Urban Information on  
1097 the Urban Thermal Environment. *Journal of Geophysical Research: Atmospheres*, 128,  
1098 e2022JD038048.

1099 Wang, X. Q., and Y. B. Gong, 2010: The impact of an urban dry island on the summer heat wave  
1100 and sultry weather in Beijing City. *Chinese Science Bulletin*, 55, 1657-1661.

1101 Wei, P., X. Xu, M. Xue, C. Y. Zhang, Y. Wang, K. Zhao, A. Zhou, S. S. Zhang, and K. F. Zhu, 2023:  
1102 On the Key Dynamical Processes Supporting the 21.7 Zhengzhou Record-breaking  
1103 Hourly Rainfall in China. *Advances in Atmospheric Sciences*, 40, 337-349.

1104 Wu, G. C., Y. Li, S. Qin, Y. N. Mao, and K. C. Wang, 2021: Precipitation Unevenness in Gauge  
1105 Observations and Eight Reanalyses from 1979 to 2018 over China. *Journal of Climate*, 34,  
1106 9797-9810.

1107 Xia, R. D., and D. L. Zhang, 2019: An Observational Analysis of Three Extreme Rainfall Episodes of  
1108 19-20 July 2016 along the Taihang Mountains in North China. *Monthly Weather Review*,  
1109 147, 4199-4220.

1110 Xian, T., J. Guo, R. Zhao, T. Su, and Z. Li, 2023: The Impact of Urbanization on Mesoscale  
1111 Convective Systems in the Yangtze River Delta Region of China: Insights Gained From  
1112 Observations and Modeling. *Journal of Geophysical Research: Atmospheres*, 128,  
1113 e2022JD037709.

1114 Yang, P., G. Y. Ren, and P. C. Yan, 2017: Evidence for a Strong Association of Short-Duration  
1115 Intense Rainfall with Urbanization in the Beijing Urban Area. *Journal of Climate*, 30,  
1116 5851-5870.

1117 Yin, J. F., D. L. Zhang, Y. L. Luo, and R. Y. Ma, 2020: On the Extreme Rainfall Event of 7 May 2017  
1118 over the Coastal City of Guangzhou. Part I: Impacts of Urbanization and Orography.  
1119 *Monthly Weather Review*, 148, 955-979.

1120 Yu, H., A. F. Prein, D. Qi, and K. Wang, 2024: Kilometer-scale multi-physics simulations of heavy  
1121 precipitation events in Northeast China. *Climate Dynamics*, 62, 9207-9231.

1122 Yu, M., and Y. M. Liu, 2015: The possible impact of urbanization on a heavy rainfall event in  
1123 Beijing. *Journal of Geophysical Research-Atmospheres*, 120, 8132-8143.

1124 Yu, M., S. G. Miao, and Q. C. Li, 2017: Synoptic analysis and urban signatures of a heavy rainfall  
1125 on 7 August 2015 in Beijing. *Journal of Geophysical Research-Atmospheres*, 122, 65-78.  
1126 Zajic, D., H. J. S. Fernando, R. Calhoun, M. Princevac, M. J. Brown, and E. R. Pardyjak, 2011: Flow  
1127 and Turbulence in an Urban Canyon. *Journal of Applied Meteorology and Climatology*,  
1128 50, 203-223.  
1129 Zhang, D.-L., Y. Lin, P. Zhao, X. Yu, S. Wang, H. Kang, and Y. Ding, 2013a: The Beijing extreme  
1130 rainfall of 21 July 2012: "Right results" but for wrong reasons. *Geophysical Research*  
1131 *Letters*, 40, 1426-1431.  
1132 Zhang, D. L., Y. H. Lin, P. Zhao, X. D. Yu, S. Q. Wang, H. W. Kang, and Y. H. Ding, 2013b: The  
1133 Beijing extreme rainfall of 21 July 2012: "Right results" but for wrong reasons.  
1134 *Geophysical Research Letters*, 40.  
1135 Zhang, W. X., K. Furtado, T. J. Zhou, P. L. Wu, and X. L. Chen, 2022: Constraining extreme  
1136 precipitation projections using past precipitation variability. *Nature Communications*, 13.  
1137 Zhang, Y. Z., S. G. Miao, Y. J. Dai, and R. Bornstein, 2017: Numerical simulation of urban land  
1138 surface effects on summer convective rainfall under different UHI intensity in Beijing.  
1139 *Journal of Geophysical Research-Atmospheres*, 122, 7851-7868.  
1140 Zhong, S., Y. Qian, C. Zhao, R. Leung, and X. Q. Yang, 2015: A case study of urbanization impact  
1141 on summer precipitation in the Greater Beijing Metropolitan Area: Urban heat island  
1142 versus aerosol effects. *Journal of Geophysical Research-Atmospheres*, 120, 10903-  
1143 10914.  
1144